Quantitative Study of Storm Surge Risk Assessment in Undeveloped Coastal Area of China Based on Deep Learning and Geographic Information System Techniques: A Case Study of Double-Moon Bay Zone

Lichen Yu [a, d], Hao Qin [*, a, d], Shining Huang [c], Wei Wei [a, d], Haoyu Jiang [a, d], Lin Mu [*, b]

[a] Hubei Key Laboratory of Marine Geological Resources, College of Marine Science and Technology, China University of Geosciences, Wuhan, China, 430074

[b] College of Life Sciences and Oceanography, Shenzhen University, Shenzhen, China, 518060

[c] Marine Information Center, Department of Natural Resources of Huizhou Bureau, Huizhou, China, 516003

[d] Shenzhen Research Institute, China University of Geosciences, Shenzhen, China, 518057

[*] Corresponding authors: Hao Qin (qh1qh100@alumni.sjtu.edu.cn); Lin Mu (moulin1977@hotmail.com).

Abstract

Storm surge is a common nature disaster in China southern coastal area, which usually causes heavy human life and economic losses. With the economic development and population concentration of coastal cities, the storm surges may result in more impacts and damage in the future. Therefore, it is of vital importance to conduct risk assessment to identify high-risk areas and evaluate economic losses. However, quantitative study of storm surge risk assessment in undeveloped areas of China is difficult, since there is a lack of building characters and damage assessment data. Aiming at the problem of data missing in undeveloped areas of China, this paper proposes a methodology for conducting storm surge risk assessment quantitatively based on deep learning and geographic information system (GIS) techniques. Five defined storm surge inundation scenarios with different typhoon return periods are simulated by coupled FVCOM-SWAN model, the reliability of which is validated using official measurements. Building footprints of the study area are extracted through TransUNet deep learning model and Remote Sensing Image (RSI), while building heights are obtained through Unmanned Aerial Vehicle (UAV) measurement. Subsequently, economic losses are quantitatively calculated by combing the adjusted depth-damage functions and overlay analysis of the buildings exposed to storm surge inundation. Zonation maps of the study area are illustrated to display the risk levels according to the economic losses. The quantitative risk assessment and zonation maps can help the government to make storm surge disaster prevention measures and optimize land use planning, and thus to reduce the potential economic losses of the coastal area.

Keywords: Strom surge; Quantitative risk assessment; GIS; Deep learning; Risk zonation map

1. Introduction

Storm surge, defined as the abnormal rise of water over and above the normal astronomical tide, and is expressed in terms of height above predicted or expected tide levels. Mostly, the surge is generated by a strong atmospheric disturbance, and it becomes particularly catastrophic when it happens to coincide with an astronomical high tide. In that case, the surge-driven coastal flooding may inundate buildings and cropland, cause significant casualties and economic losses. Storm surges have caused widespread damage worldwide. In 2013, super typhoon Yolanda as the worst

45 typhoon in last 30 years, pounded the Philippines. It caused 6293 individuals reported dead, 28689
46 injuries and 1061 individuals missing, with estimated damages totaling 864 million US dollars
47 (Mcpherson, 2015). Hurricane Harvey struck Texas in August 2017, resulting in approximately
48 100 deaths and economic losses exceeding 125 billion dollars (Lee, 2021). In China, storm surges
49 also pose a frequent threat in the coastal cities. In the last decade, China has experienced an
50 average of 8.5 storm surge disasters annually, with an average damage amount of 6815.8 million
51 yuan per year, where Guangdong and Zhejiang Provinces are the most affected coastal areas
52 (China Marine disaster bulletin, 2022). For example, Typhoon Hato in 2017, Typhoon Mangkhut
53 in 2018, Typhoon Lekima in 2019 has caused significant damage to coastal cities in China, and
54 resulted great losses of life and property (Zhou et al., 2021; Yang et al., 2019). For the past few
55 years, as the rapid development of population and economic in China coastal area, the potential
56 monetary loss grows accordingly (Fang et al., 2021; Ji et al., 2020; Mcgranahan et al., 2007; Seto
57 et al., 2011). Therefore, it is crucial to implement risk assessment and mapping strategies to
58 effectively reduce these risks and mitigate the impact of storm surges.

59   Storm surge hazard assessment is an essential component of storm surge risk assessment and
60 zoning, aiming to evaluate the hazard intensity of disasters, through numerical simulation of storm
61 surge processes, estimation of storm surge for selected return periods, and computation of the
62 probable maximum storm surge (Shi et al., 2013). Therefore, the numerical simulation of storm
63 surge is a key step for storm surge risk assessment. Because of the limitation of historical storms
64 and the nondeterminacy of future storm, numerical simulation of storm surges is usually used to
65 determine storm levels. Hydrodynamic model such as Advanced Circulation Mode (ADCIRC),
66 Delft3D and Finite Volume Coastal Ocean Model (FVCOM) have been widely used (Vijayan et al.,
67 2021; Wang et al., 2021a; Liu and Huang, 2020; Hu et al., 2022; Lyddon et al., 2019; Zhang et al.,
68 2020; Zhu et al., 2022). It has been demonstrated that it is critical to include tide and sea-water-
69 level variations in shelf and nearshore wave simulations (Masson, 1996). Furthermore, the sea
70 water level could be significantly affected by strong tide and typhoon-induced wind in complex
71 coastal seas and then modulate the wave properties (Yang et al., 2020). Coupled FVCOM-SWAN
72 model, with the foundation of FVCOM's finite volume method, unstructured grid, and adaptable
73 boundary condition handling capability, integrating the hydrodynamic and wave processes of
74 SWAN, possesses the ability to provide simulation result more quickly and accurately. In this
75 circumstance, coupled FVCOM-SWAN model is used in this research for simulating the
76 inundation of storm surge.

77   Coastal risk assessment can be categorized into two primary classifications: qualitative and
78 quantitative. In the realm of qualitative assessment, entropy weight method, Analytic Hierarchy
79 Process (AHP) and other methods are widely used. Ramkar and Yadav (2021) used AHP in
80 combination with Geographic Information Systems (GIS) for proposing a flood risk map, which
81 can identify the high-risk areas efficiently. Malekinezhad et al. (2021) combined the entropy
82 weight method and GIS, and conducted a flood vulnerability analysis for Hamadan city. The
83 results highlighted the advantages of entropy weight method comparing to normal spatial overlay
84 method. Besides, Pathan et al. (2022) and Rafiei-Sardooi et al. (2021) made use of Technique for
85 Order Preference of Similarity by Ideal Solution (TOPSIS). The former pointed out the
86 advancement of TOPSIS by comparing with AHP, and the latter combined machine learning and
87 TOPSIS to analyze urban flood vulnerability. Unlike qualitative risk assessment, quantitative risk
88 assessment enables the quantification of damages and risks in monetary terms. The most

89 commonly used approach to assess direct damages is based on depth-damage curves (De Moel and
90 Aerts, 2011; Merz et al., 2007; Smith, 1994). Thieken et al. (2008) presented the Flood Loss
91 Estimation Model for the private sector (FLEMOps) through using the Germany flood losses data
92 in August 2002, and the group further established model for commercial sector in 2010 (Kreibich
93 et al., 2010). Zhai et al. (2005) derived multi-factor loss functions for buildings in Nagoya, Japan
94 using empirical data from Tokai flood in 2000, and Grahn and Nyberg (2014) established
95 functional relationships utilizing the house insurance claims data caused by lake flooding. Except
96 for buildings, Yazdi and Salehi Neyshabouri (2012) and Hess and Morris (1988) respectively built
97 several uni-variable functions and multi-factor functions for kinds of crops and grassland. In
98 recent years, machine learning is also introduced in quantitative loss assessment, for example,
99 Merz et al. (2013) developed a tree-based approach using Regression Tree and Bagging
100 Regression Tree as machine-learning methods to analysis of direct building damage to private
101 homes. Paprotny et al. (2020) proposed a Bayesian Network damage model (a supervised-
102 machine-learning method), and reached a good accuracy of predictions of building losses.

103   The essence of quantitative risk assessment lies in analyzing the interaction between
104 exposure factors and hazards (Adnan et al., 2020; Armenakis and Nirupama, 2013; Granger, 2003;
105 Kron, 2005). Therefore it's crucial to quantify the direct tangible damage of elements at risk.
106 Buildings are important exposure elements, as they are the gathering place of population and
107 property. Building footprint data is necessary for evaluating the vulnerabilities of a building, as it
108 provides essential information about the buildings, including spatial location, distribution, and
109 boundaries and so on (Mharzi Alaoui et al., 2022). It's also of great significance in risk assessment,
110 primarily due to its ability to identify high-risk areas, assess building vulnerability and estimate
111 potential damage (Gacu et al., 2023; Wu et al., 2019). Extracting building footprints from remote
112 sensing images has been widely used in many fields, such as urban management, disaster
113 management, navigation (Zhou et al., 2004; Tang et al., 2006; Liu et al., 2019; Liu et al., 2020;
114 Rousell and Zipf, 2017; Chen and Gao, 2019). However, there is a lack of building footprints
115 extraction and application in the realm of storm surge assessment.

116   When the building is inundated, there are a variety of factors that may influence the amount
117 of monetary loss. For example, building type, building structure, private precaution, maintenance
118 status, and others (Marvi, 2020; Thieken et al., 2008). Taramelli et al. (2022) pointed out that
119 building's height is one of the factors for determining the susceptibility due to flooding and
120 evaluate the buildings' potential damage by flood hazards. Hasanzadeh Nafari et al. (2016)
121 developed a new loss model, in which building with different story were divided into different
122 categories in the modelling process. To conclude, height is an important factor that affecting the
123 vulnerability of buildings when they serve as inundation-exposed elements. Therefore, in the
124 process of quantitative storm surge risk assessment, it is necessary to adjust the depth-damage
125 functions to make buildings of different heights correspond to different functions.

126   Besides, different from the field research and statistics required for other data acquisition, the
127 data of buildings' height is more accessible from multiple sources. For example, public data DSM
128 data has been utilized for building height estimation (Huang et al., 2022), some satellite companies
129 also offer services to customize DSM data for selected regions. Nonetheless, they respectively
130 suffer from a lack of precision and high costs. Building height can also be obtained via remote
131 sensing technique, such as Synthetic Aperture Radar (SAR) (Li et al., 2020; Frantz et al., 2021), or
132 take advantage of shadow in remote sensing images (Comber et al., 2011; Shao et al., 2011).

However, in addition to the lack of precision, the absence of data necessary for modelling and the crowded character of rural buildings in China make the above methods difficult to be implemented. Compared to methods above, acquiring building height through UAV ensures high accuracy while being relatively efficient, and the method is quite simple, which also reduces the required costs.

In view of the aforementioned information, regarding storm surge qualitative risk assessment, there is a stringent requirement for both the quality and timeliness of land use data, which means that the risk assessment cannot be generated in real time, and the qualitative risk assessment also can't evaluate the risk level through the intuitive value of economic loss. In the realm of quantitative risk assessment, building a uni-variable or multi-factor empirical model requires complete and substantial data, and the published models generally only provide uni-variable functions ignoring the building height as a factor, or have regional limitations. Additionally, for the coastal regions of China, which are often affected by storm surge disasters, they tend to have relatively low levels of economic development. Under the circumstances, the data needed to conduct flood risk assessment is generally in a state of absence.

In response to the challenges mentioned above, the scientific goal of this paper is to propose a quantitative storm surge risk assessment method for underdeveloped areas based on deep learning and GIS techniques. First, on the basis of high-resolution DEM and seawall data measurement, five defined storm surge inundation scenarios with different typhoon return periods are simulated by employing the coupled FVCOM-SWAN model. Subsequently, TransUNet is introduced as a deep learning method to extract building footprint, and building's height data is acquired through UAV measurement. Since data on relevant disaster losses in underdeveloped regions are lacking, empirical modeling was deemed impractical. Therefore, the adjustment of the JRC's depth-damage curves by the HAZUS is chosen to take the impact building's height into consideration, thus to conduct a quantitative assessment with more accuracy. Finally, combining hazard map, exposure elements and adjusted depth-damage curves, the quantitative risk zoning maps are conducted. The risk zoning maps can assist decision-makers in identifying high-risk sub-zones and planning disaster prevention measures. Accordingly, the novelty can be seen in obtaining refined exposure elements data through deep learning and UAV, addressing the lack of historical storm surge economic loss data and considering the effect of building height on economic loss through the adjustment of existing depth-damage curves.

2. Study area and datasets

2.1. Study area

Being the shipping hub in the South China Sea, Guangdong province, located in southern China, has become the largest economic province in China since 1989, with a GDP of 129118.6 billion yuan in 2022. Due to the seaborne trade, Guangdong has been the largest economic province in China since 1989, which reached a GDP of 129118.6 billion yuan in 2022. However, just as mentioned above, Guangdong is relatively vulnerable to storm surges, such as Typhoon Hato and Typhoon Mangkhut, due to its geographical characteristics.

Huizhou is one of the cities in Guangdong province, and also one of the central cities of Pearl River Delta region. It's located at on the east coast of Guangdong-Hong Kong-Macao Greater Bay Area, the GDP reached 540.1 billion yuan in 2022, with the highest growth rate in Guangdong. Pinghai Town located at the southernmost of Huizhou, and has a registered population of about forty thousand. Its economic source mainly depends on various crops and seafood products. Due to its coastal geographical characteristics and the presence of Pinghai Ancient City, the town has

177 become a cultural tourist destination and can therefore be defined as a cultural tourist town.

178   In this paper, the chosen study region is the coastal area of Pinghai town, named the Double-
179 Moon Bay Zone. It covers ten villages in total, including Foyuan, Dayuan, Yuye, Xinliao, Xin
180 village, Shazuiwei, Cajia, Nanshe, Daao, and Harbor community. These years, the region has been
181 developed in tourism and real estate project development including construction of hotels, resorts,
182 and high-end business districts, which vastly prompt the financial development. It is foreseeable
183 that the population and economy of the region will growth rapidly. However, the economic status
184 of the region remains relatively low, which presents a challenge due to data scarcity and limited
185 accessibility. In addition, the region is susceptibly affected by the tropical cyclones during the
186 season running from April to November (Wang et al., 2021b). Recent years, more than ten
187 typhoons have affected the study area, including Typhoon Lekima, Typhoon Haishen, Typhoon
188 Kanuni etc. The general location and information about the study area is shown on Fig. 1.
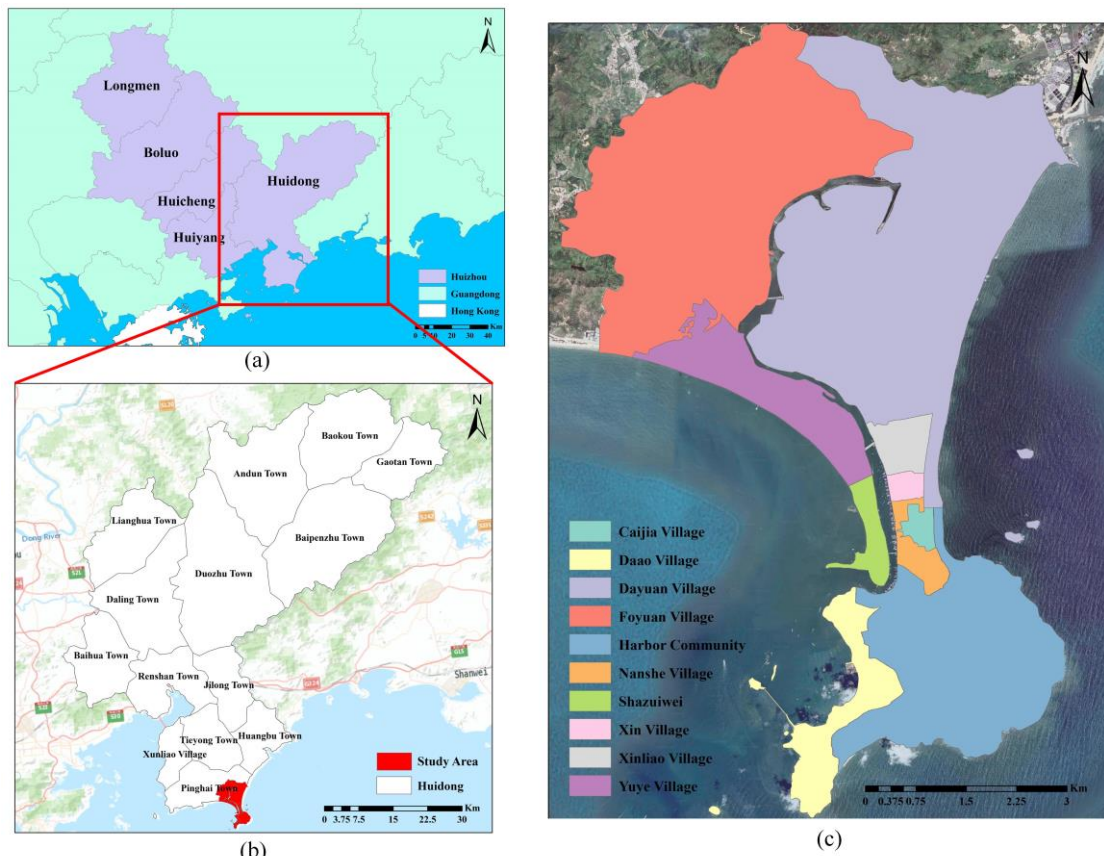
189
190 **Fig. 1.** The maps of locations in the study: (a) The map of Huizhou; (b) The map of study area in
191 Huidong, the base map is obtained from ESRI; (c) The village map of study area, the base map is
192   obtained from © GoogleMaps (map data © 2023 Google).

193
194 *2.2. Data source*

195   In order to accomplish the research, the data used is obtained from various sources, here is
196 the describe of different data:

197   (1) Land Cover Types data: the data is obtained from the Department of Natural Resources of
198 Huizhou Bureau. It contains multiple land cover types including forest, cropland, residential land,
199 etc. It is used to calculate vulnerability level.

200   (2) Remote sensing images: the remote sensing images are obtained from Chang Guang Jilin-

1 satellite. Chang Guang Satellite technology CO., LTD was founded on December 1st 2014, which is the first and the largest commercial satellite corporation in China. Jilin-1 is the first self-developed commercial high-resolution satellite. The images from Jilin-1 satellite have a resolution of 50 cm, and have five spectral channels: Panchromatic band; Blue band; Red band; Green band; Near Infrared band. The images consisting of blue band, red band, green band are utilized to combine deep learning method, thus achieve the extraction of buildings.

(3) Unmanned Aerial Vehicle (UAV) data: the UAV data is generated by oblique photography, and is organized by Open Scene Graph Binary format. The UAV data is obtained from Department of Natural Resources of Huizhou Bureau, and the data is utilized for buildings' height calculation.

(4) Digital elevation model (DEM) data: the DEM data is captured by manual observation in 2018, with the resolution of 0.3m. The coordinate system and file organization are originally CGCS 2000 and txt file, and further transformed to WGS 1984 and raster format to make use of these data in the research. The data contains the elevation information for the study region. Besides, the seawall data is also obtained manually. Both data are used in modeling of storm surges for simulating the hazard maps.

(5) Hybrid wind field: ERA5 is the fifth generation of the European Reanalysis dataset produced by the European Centre for Medium-Range Weather Forecasts (ECMWF), and it provides the comprehensive and high-resolution atmospheric and climate data. Holland typhoon wind field model was proposed by Holland in 1980, which introduced Holland B parameter on the basis of the Schloemer exponential pressure distribution model (Holland, 1980). In this study, the two data are fused to generate hybrid wind field data, which is subsequently utilized for storm surge simulations.

(6) Historical typhoon data: the historical typhoon data including typhoon track, typhoon pressure, and velocity are obtained through China Meteorological Administration Typhoon Network Website. The historical data is employed to assess the reliability and validity of the model.

(7) Administrative Boundary data: the data is obtained from National Platform for Common Geospatial Information Services, and it contains administrative boundaries at village level. There are ten villages in the study area.

3. Method

The methods in this study aim to assess quantitative direct tangible damage over the study area consists of following steps: hazard assessment; exposure assessment; vulnerability assessment; risk assessment, and the flowchart of the procedure is illustrated in Fig. 2.

First, with respect to hazard assessment, five storm surge scenarios are defined. After constructing wind field through Holland model, the inundation area and depth of different typhoon return periods are simulated by utilizing the coupled FVCOM-SWAN model. In exposure assessment, building footprints and heights are extracted by introducing a deep learning method TransUNet and shadow calculation. Then the hazard maps are overlaid to identify the elements at risk. Considering the effect of building's floor in flood monetary loss estimation, the JRC's depth-damage functions are adapted representing the vulnerability of different exposed elements. Eventually, the economic loss of different typhoon scenarios can be summarized and the risk assessment is conducted through multiplying the temporal probability. Moreover, the quantitative zoning maps of four risk levels are generated through zonal statistic.
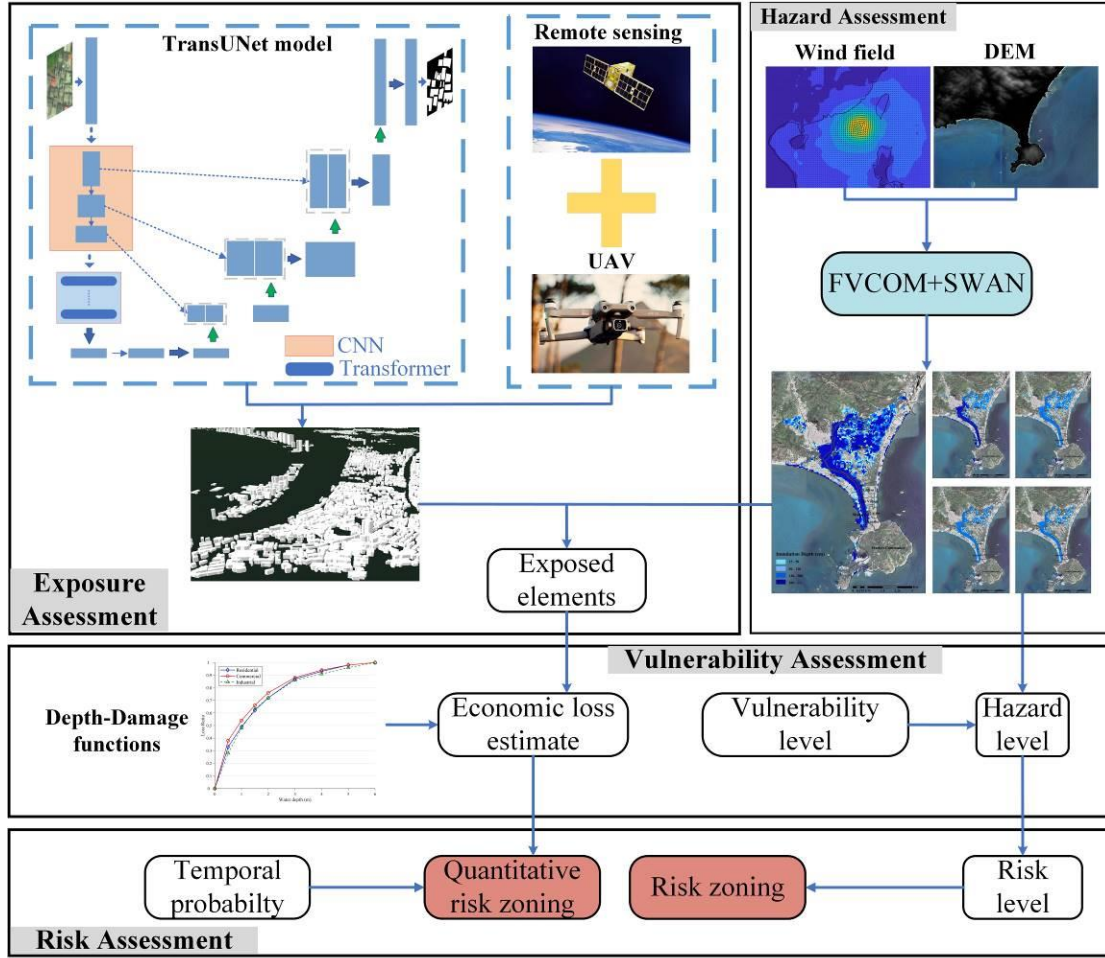
Fig. 2. The flowchart of the presented storm surge quantitative risk assessment method. The base map is obtained from © GoogleMaps (map data © 2023 Google).

3.1. Strom surge inundation simulation

Finite Volume Coastal Ocean Model (FVCOM), is a coastal ocean circulation model, which was originally developed by Chen et al. (2003), and further improved by the University of Massachusetts and the Woods Hole Oceanographic Institution. The following are the governing equations of FVCOM, comprising momentum, continuity, temperature, salinity, and density equations:

$$\frac{\partial u}{\partial t} + u\frac{\partial u}{\partial x} + v\frac{\partial u}{\partial y} + wfv = -\frac{1}{\rho_o}\frac{\partial P}{\partial x} + \frac{\partial}{\partial z}\left(K_m\frac{\partial u}{\partial z}\right) + F_u \tag{3.1}$$

$$\frac{\partial v}{\partial t} + u\frac{\partial v}{\partial x} + v\frac{\partial v}{\partial y} + w\frac{\partial v}{\partial z} + fu = -\frac{1}{\rho_o}\frac{\partial P}{\partial y} + \frac{\partial}{\partial z}\left(K_m\frac{\partial v}{\partial z}\right) + F_v \tag{3.2}$$

$$\frac{\partial P}{\partial z} = -\rho g \tag{3.3}$$

$$\frac{\partial u}{\partial x} + \frac{\partial v}{\partial y} + \frac{\partial v}{\partial z} = 0 \tag{3.4}$$

$$\frac{\partial T}{\partial t} + u\frac{\partial T}{\partial x} + v\frac{\partial T}{\partial y} + w\frac{\partial T}{\partial z} = \frac{\partial}{\partial z}\left(K_h\frac{\partial T}{\partial z}\right) + F_T \tag{3.5}$$

$$\frac{\partial S}{\partial t} + u\frac{\partial S}{\partial x} + v\frac{\partial S}{\partial y} + w\frac{\partial S}{\partial z} = \frac{\partial}{\partial z}\left(K_h\frac{\partial S}{\partial z}\right) + F_S \tag{3.6}$$

$$\rho = \rho(T, S) \tag{3.7}$$

255 Where x, y and z respectively represent the east, north and vertical coordinate axes in the
256 Cartesian coordinate system; u, v and w are the velocity components in x, y, z directions; T,
257 S and ρ are the temperature, salinity and density; P is the pressure and f stands for the
258 Coriolis parameter; K_m is the vertical eddy viscosity coefficient and K_h is the vertical eddy
259 diffusivity coefficient for heat; g is the gravitational acceleration; F_u, F_v, F_T, and F_S are the
260 horizontal diffusion terms.

261 Simulating Waves Nearshore (SWAN) is the third-generation offshore wave model developed
262 by Delft University of Technology and it was originally proposed by Booij et al. (1996). The
263 governing equation of the model is shown as

$$\frac{\partial}{\partial t}N + \frac{\partial}{\partial x}C_x N + \frac{\partial}{\partial y}C_y N + \frac{\partial}{\partial \gamma}C_\gamma N + \frac{\partial}{\partial \theta}C_\theta N = \frac{S}{\gamma} \tag{3.8}$$

264 Where N is the wave action density; θ is the propagation direction; C_x, C_y are respectively
265 the x, y components of propagation speed and C_γ, C_θ are the γ, θ components of propagation
266 cospeed; γ and S respectively represent the frequency and the source term for the wave energy.

267 The potential storm surge inundation maps in different typhoon scenarios have been
268 conducted by institutions such as the National Oceanic and Atmospheric Administration (NOAA),
269 National Hurricane Center, and other departments since the 1990s (Glahn et al., 2009). In the field
270 of risk assessment research, it is common to set up different typhoon scenarios using storm surge
271 simulation models to obtain various scenarios of typhoon induced inundation (Zhang et al., 2023;
272 Rizzi et al., 2017). The hazard maps of under various typhoon intensity scenarios are helpful for
273 decision-makers and researchers in analysing multiple aspects of potential hazards in the study
274 area.

275 Typhoon Mangkhut, as one of the largest typhoons to affect South China Sea region in recent
276 years, has a strong representative. It is characterised by high intensity, wide area of influence, high
277 wind speed, etc. In this study, the path of Typhoon Mangkhut is shifted to pass through the
278 Huizhou tidal station as the input typhoon path of the coupled model to maximize the impact area
279 of the simulation result. In terms of the center pressure, Wang et al. (2021b) presented statistical
280 analyses of historical typhoon data in Huizhou, and designed five typhoon scenarios, which are
281 respectively the typhoon minimum central pressure of 880, 910, 920, 930 and 940 hPa. Therefore,
282 these five parameters are introduced as the setup for five typhoon scenarios.

283 FVCOM and SWAN both use the unstructured triangular grid to subdivide the South China
284 Sea, and the latitude and longitude range of the region is 13°N - 29°N, 109°E-122°E. The SWAN
285 parameters are set as follows: wind input growth term and whitecap dissipation term are the
286 Komen scheme; Bottom friction dissipation is parameterized using the Madsen vortex viscosity
287 model; The nonlinear interactions are implemented using three-wave and four-wave nonlinear
288 interaction schemes. The input wind field is the fusing wind field derived from ERA5 and the
289 Holland method. The open boundary forced tidal elevation of FVCOM is conducted by calculating
290 the harmonic constants for the eleven major astronomical tidal constituents, namely M2, N2, S2,
291 K2, K1, O1, P1, Q1, MS4, M4, and M6. The forcing field is the fusing wind field and the wave
292 data generated by SWAN. The external model time step for the model is set to 0.75 second, while
293 the internal model time step is set to 7 seconds.

294   In summary, FVCOM-SWAN coupling method is utilized for simulating the inundation
295 caused by storm surge. Specifically, following the modification of typhoon Mangkhut's central
296 pressure, velocity, and track data, the data is utilized as input for the Holland typhoon wind field
297 model, subsequently yielding the wind field outcome. The hybrid wind field data generated is fed
298 into the SWAN model to generate wave data. Then, both the wind data and wave data are input
299 into the FVCOM model to calculate the extent of inundation.
300
301 *3.2. Buildings extraction*
302   The deep learning model used in the research is TransUNet (Chen et al., 2021), which was
303 originally proposed for medical images segmentation. TransUNet incorporates transformer in
304 encoder within the architecture of U-shape network, consequently makes use of the advantage of
305 global information extraction while fusing the superficial and deep features. On the mission of
306 building extraction, the target is to segment the building's area precisely. The TransUNet model
307 can effectively identify the boundary between buildings and background, which enables the model
308 to be competent for extracting the buildings in different size and shape.
309   The following is relevant introduction of the structure of the model.
310 *3.2.1. Transformer in TransUNet*
311   Transformer was first proposed by Sutskever et al. (2014), which was originally utilized for
312 machine translation. However, as more variants of transform were developed, people found
313 transform also perform well in multiple tasks, such as natural language processing (NLP),
314 computer vision (CV) and automatic speech recognition (ASR).
315   The transformer encoder is composed of L layers of Multi-head Self-Attention (MSA), Layer
316 normalization (LN) and Multi-Layer Perceptron (MLP), the structure is shown in the Fig. 3(a), and
317 the equations of Query-Key-Value (QKV) self-attention and MSA are shown below:

$$\text{Attention}(Q,K,V) = \text{softmax}(\frac{QK^{\text{T}}}{\sqrt{D_k}})V \tag{3.9}$$

$$\text{MultiHeadAttn}(Q,K,V) = \text{Concat}(\text{head}_1,...,\text{head}_H)\mathbf{W}^O \tag{3.10}$$

$$\text{head}_i = \text{Attention}(QW_i^Q, KW_i^K, VW_i^V) \tag{3.11}$$

318   Where Q, K, V are respectively the Query, Key, Value vector. $\sqrt{D_k}$ is the scaled dot- -
319 product attention. $\mathbf{W}^O$, W_i^Q, W_i^K, W_i^V are respectively the corresponding linear mapping, which
320 convert Q, K, V and the output to the specified dimension.
321   The MSA has a positive effect on helping the model identify the target objects and
322 background, thus the neutral network can learn more information form the target. LN is deemed to
323 stabilize the deep network training, which can prevent unstable gradient, model degradation, etc.
324 The module receives the 2d flatted patches from the image's patches. Due to it is different from
325 CNN or RNN, apart from map the vectorized patches to D-dimensional embedding space,
326 transformer needs to apply additional position encoding for retaining the patch's positional
327 information.
328 *3.2.2. Structure of TransUNet*
329   The overall structure of TransUNet is reference to U-Net, which is a U-shaped Encoder-
330 Decoder structure, and the structure diagram is shown in the Fig. 3(b).
331   Encoder: the origin image is put into the CNN part for feature extraction, after the processing
332 of position encoding and flatten, the patches are further put into the transformer module. The

transformer module consists of 12 transformer layers. The CNN part is implemented through using resnet50, which include 3 blocks in total, and each block output the hidden feature for skip connection.

Decoder: reshape the output sequence from encoder and then cascade up-sampling after transforming the number of channels. During the process, the skip connection is introduced by using the feature map hereinbefore. In the end, the segmentation result is generated.

In conclusion, TransUNet is the combination of U-Net and transformer, which is designed to make use of the advantage from both structures. The Global Attention from transformer can contribute to learn the global information, while the skip connection from U-shape network can contribute to get more information from shallow feature map output from CNN, and also CNN performs better in extracting the local information. In this research, buildings images are similar to medical images, with the features like high complexity level, large range of gray values. The skip connection structure can simultaneously acquisition of low-level semantic features and high-level semantic features, and transformer can conduce identify the buildings from background, thus TransUNet achieves a high accuracy in buildings segmentation.

(a)   (b)
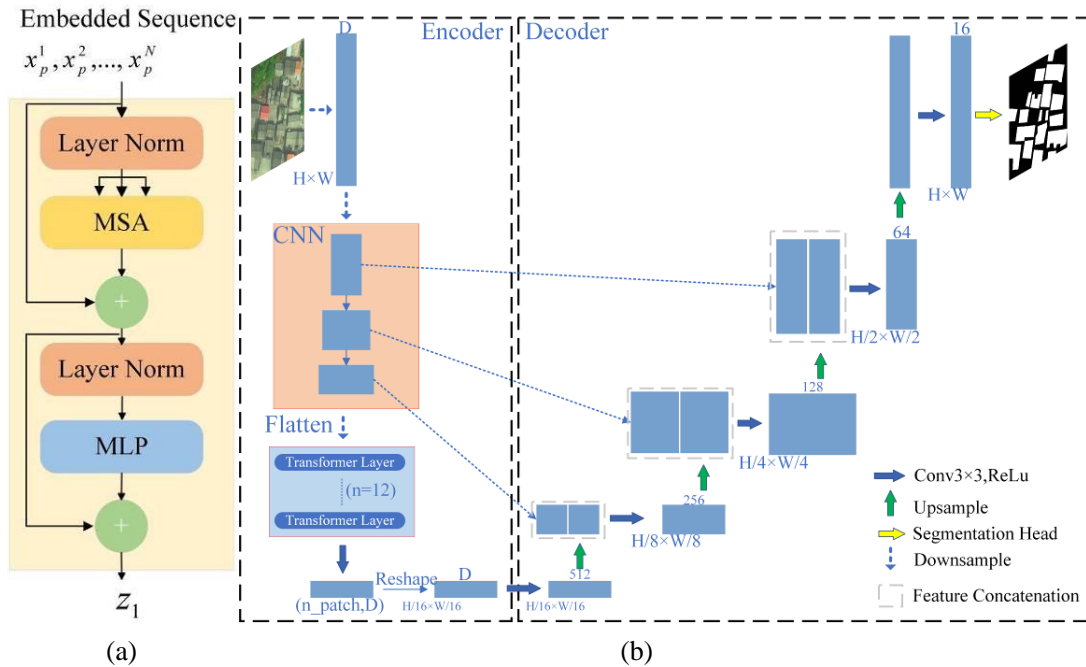
Fig. 3. The overview of TransUNet framework (adapted from (Chen et al., 2021)): (a) Schematic diagram of Transformer layer; (b) Structure diagram of TransUNet

3.3. Building's height acquisition

UAV tilt photography modeling technology can combine control points encryption from massive image data with a small number of ground control points to obtain accurate external orientation elements (Kang et al., 2020). The conducted 3D model reflects the truly condition of the ground, and the data is selected to be in the WGS 1984 coordinate system. The ground resolution is one of the most intuitive and important parameters in tilt photography, and it's also a key factor determining the quality of the 3D modeling. In the process of performing aerial triangulation for tilt-image automation, it is necessary to ensure that the resolution of the different images is as consistent as possible while taking into account the resolution of the side-view image, thus to ensure accuracy and image overlap. Hence, the combinatory analysis of image resolution at

tilted viewing angle is required. The tilted image center point, near point and far point resolutions are expressed as follows:

$$\text{GSD}_{\text{top}} = \frac{\delta h \cos \beta_y}{f \cos(\alpha_y - \beta_y)} \tag{3.12}$$

$$\text{GSD}_{\text{mid}} = \frac{\delta h}{f \cos \alpha_y} \tag{3.13}$$

$$\text{GSD}_{\text{bottom}} = \frac{\delta h \cos \beta_y}{f \cos(\alpha_y + \beta_y)} \tag{3.14}$$

Where δ is sensor cell size, h is flight height, f refers to the camera focal length, α_y and β_y are respectively dip angle and half the angle of view. Normally, the ground resolution at the center of the tilted and vertical images should be comparable, and the minimum resolution of tilted images should less than three times the resolution of a vertical image.

There are multiple formats available for storing 3D models, including OBJ, STL, FBX, OSGB, etc. In this study, the generated 3D model is saved as OSGB format. OSGB format is originally proposed by Ordnance Survey for storing the geographic spatial data in the British. It combines binary encoding and compression algorithms to improve the data storage and transmission efficiency. Normally, the OSGB data contains information of geographic coordinates, elevations, texture mapping, and geometric shapes, which can be used to GIS application, virtual reality (VR), among others.

Digital surface model (DSM) is a digital terrain model that contains elevation information about trees, buildings, and bridges. Compare to DEM, DSM can reflect the truly surface condition of earth, thus DSM has a wide range of application in city management or forest stewardship. In this research, the UAV data can be transformed to DSM data by using SuperMap software, and the DSM result is shown in Fig. 4(b). After generating the DSM, the elevations of the roof of the buildings and the corresponding elevations of the ground around the buildings are extracted by manual selection, then the height of buildings can be calculated by using equation (3.15).

$$DSM_{Roof} - DSM_{Ground} = H \tag{3.15}$$

Where DSM_{Roof} is the DSM value of the building's roof, DSM_{Ground} represents the corresponding DSM value of ground, and H is the result of building's height.

(a)   (b)
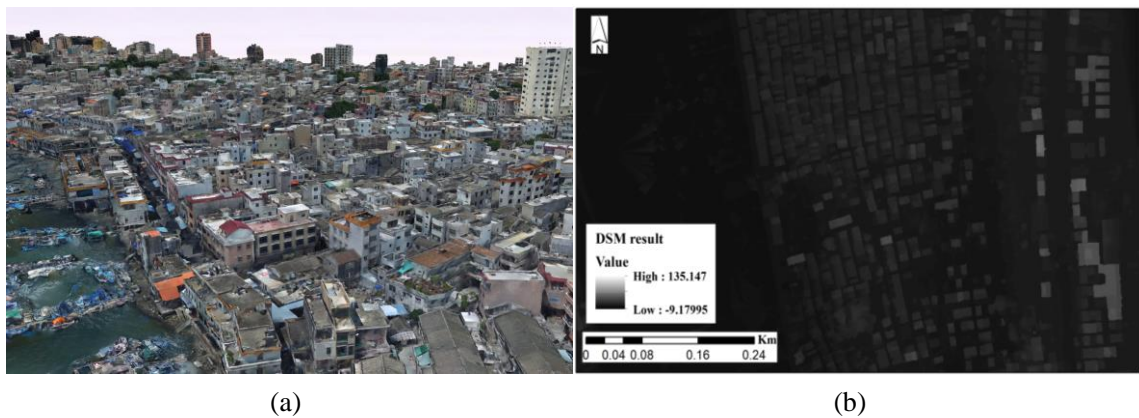
Fig. 4. Building's height acquisition: (a) The schematic diagram of UAV tilt photography data; (b) The generated DSM results for Building height data extraction.

3.4. Exposure and vulnerability assessment

390 The process of storm surge risk assessment involves two key components: exposure and
391 vulnerability. The exposure represents the elements exposed to hazardous spaces, while the
392 vulnerability refers to the level of the exposure elements' susceptibility to damage. When doing
393 exposure assessment, the disaster-affected elements can be conducted by overlaying the building
394 footprint data and land cover data with the hazard layer, which is the inundation data in this
395 research. The process can be accomplished using overlay analysis in ArcGIS software.

396 *3.4.1. Adaptation of flood vulnerability functions.*

397 Constructing an empirical stage-damage curve is a commonly used method for conducting
398 vulnerability assessments. However, as is mentioned above, China lacks of the data about flood
399 loss or insurance compensation in flood disasters, as a result, it's not practicable to develop
400 exclusive functions for the study region, so the depth-damage functions developed by Huizinga,
401 Joint Research Center (JRC) (Huizinga et al., 2017) are introduced. The depth-damage functions
402 manifest the loss ratio of the exposure elements in different inundation depth from 0 to 6 m, and
403 the ratio range from 0 to 1, which represents no damage to fully damaged. Besides, JRC also
404 provides the maximum economic losses per square meter for six different exposure element types
405 including residential, industrial, infrastructure, road, agricultural land, and transport. In this study,
406 the original functions and maximum loss data for China region are used, and the economic loss
407 can be calculated by multiplying the loss ratio, the maximum loss, and the disaster-affected area.

408 However, the JRC's vulnerability functions do not provide the specific function of each
409 height category. In this case, the depth-damage functions in HAZUS are introduced. HAZUS is
410 first released for earthquakes in 1997 by Federal Emergency Management Agency (FEMA), and
411 that's when the HAZUS Flood Model started to be developed (Scawthorn et al., 2006). In 2004, a
412 multi-hazard version called HAZUS-MH was a standardized GIS-based model that included the
413 earthquake, flood, and hurricane models (Nastev and Todorov, 2013). The HAZUS-MH flood
414 model is designed primarily for local and regional hazard planners and emergency managers for
415 developing emergency management plans and mitigation strategies (Tate et al., 2015). However,
416 the depth-damage functions in HAZUS-MH are restricted to regions within America, hence the
417 HAZUS's functions are introduced to adapt JRC's functions.

418 The approach to modifying functions is refered to the method proposed by Dabbeek et al.
419 (2020). In the process, the HAZUS loss ratios of each height category (one-story, two-story, three
420 and more-story) are averaged, which is shown in equation (3.16). Then the contribution of each
421 height category relative to the average loss is calculated as equation (3.17) shows. In the end,
422 multiplying the value obtained in the previous step by JRC's vulnerability functions yields the
423 adapted functions for each height category.

$$\bar{D}_{i(hazus)} = \frac{d_{i,1} + d_{i,2} + d_{i,3+}}{n}$$

(3.16)

$$i(depth) = \{(0,6)\}$$

$$c_{i,h} = \frac{d_{i,h}}{\bar{D}_{i(hazus)}}$$

(3.17)

$$d_{i,h(adapted)} = c_{i,h} \times \bar{D}_{i(jrc)}$$

(3.18)

424 Where $d_{i,h}$ represents to the loss ratio at the inundation depth i for each height category h.
425 $\bar{D}_i$ is the average loss ratio of all heights.

426

427   *3.4.2. Quantitative risk assessment*

428   The quantitative financial loss estimation is accomplished by overlaying the following data:

429   the inundation simulation result generated by FVCOM and SWAN modeling, the spatial

430   distribution of three types of exposure elements, the depth-damage functions of industrial and

431   commercial elements, and the adapted depth-damage functions for residential elements in three

432   height categories. The process of loss estimation can be shown in the following equation:

$$C = \sum_{i=1}^{i=n} D_{x(i)} f(d_i) A_i \tag{3.19}$$

433   Where C stands for the economic loss estimation result. n represents the total number of

434   exposure elements. $x(i)$ is the type of the i-th element and $D_{x(i)}$ is the maximum loss of the i-th

435   element. d_i is the depth of submergence of the i-th element and $f(d_i)$ is the loss ratio of the i-th

436   element. A_i refers to the area of the i-th element.

437   Comparing to the 984 euros per m^2 monetary loss of residential buildings in 2010, the

438   monetary loss of infrastructure and agriculture are respectively 12 euros per m^2 and 0.02 euro per

439   m^2 according to JRC, only account for 1% or less. Therefore, the monetary loss estimate of

440   infrastructure and agriculture is excluded in the study.

441   In this research, five storm surge scenarios are settled, ten administrative sub-zones are given

442   four different risk levels for each defined typhoon scenario.

443

444   **4. Results and discussions**

445   *4.1. Validation*

446   The performance of coupled FVCOM-SWAN model is evaluated. Four typical typhoons

447   (Vicente, Hato, Mangkhut, Khanun) are selected to validate the coupled model for the study region.

448   The measured data of each typhoon are captured by Department of Natural Resources of Huizhou

449   Bureau. Fig. 5 shows the maximum predicted water level and highest measured water level of the

450   chosen typhoons. Relative error and absolute error are introduced to evaluate the model and Table

451   1 displays the statistical results from Huizhou tidal station. It is seen that the predicted results are

452   in good agreement with the measurements. The statistic result shows that the relative errors of the

453   four typhoons range from 2.1% to 19.8%, and the absolute error varies from 4 cm to 54 cm.

454   Therefore, the coupled FVCOM-SWAN model demonstrates a reliable competence in

455   accomplishing the storm surge simulation task.
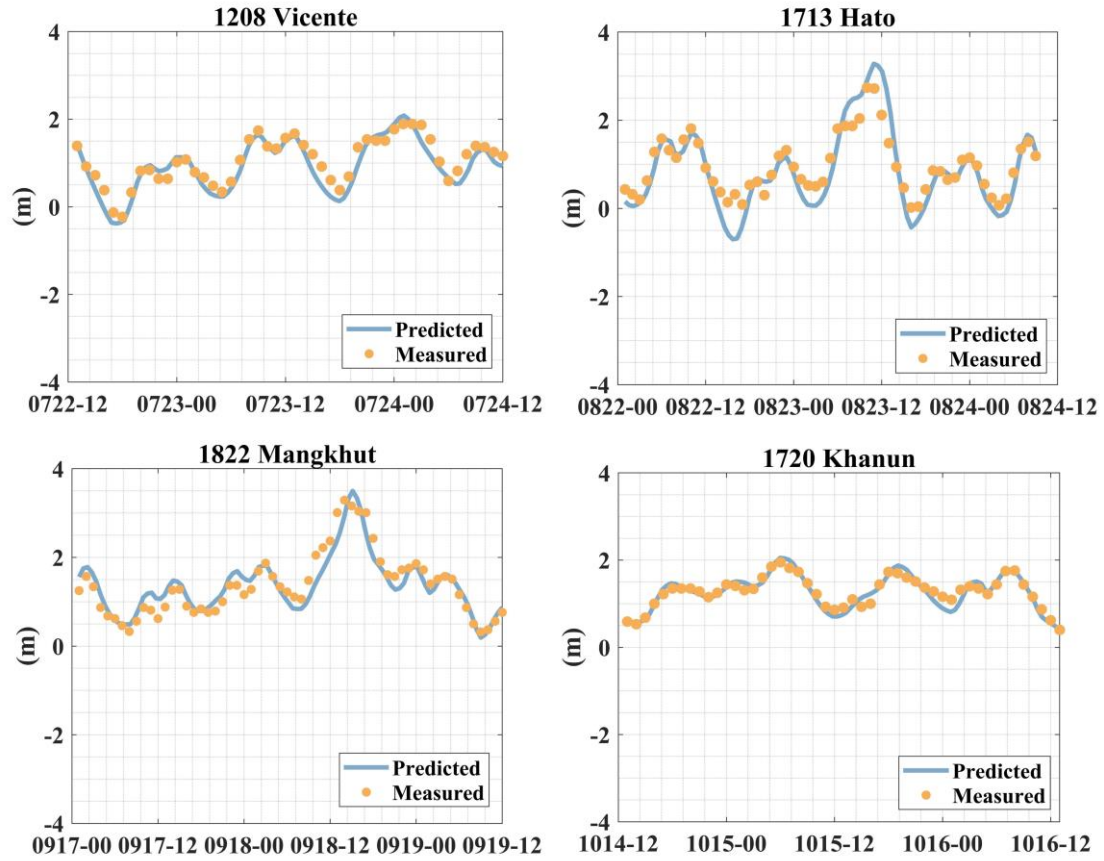
Fig. 5. The predicted water level and highest measured water level recorded by Huizhou tidal station during different typhoon event

Table 1. The Relative error and Absolute error between maximum predicted water levels and highest measured water levels from Huizhou tidal station during different typhoon events

Typhoon name	Measured data (cm)	Relative error (%)	Absolute error (cm)
Vicente (1208)	189	10.3	19
Hato (1713)	274	19.8	54
Mangkhut (1822)	329	6.5	22
Khanun (1720)	201	2.1	4

4.1. Hazard assessment

In the present research, five storm surge inundation scenarios are defined, which represent five different typhoon return periods: 10-year, 20-year, 50-year, 100-year, 1000-year respectively corresponding to minimum central pressure 940hPa, 930hPa, 920hPa, 910hPa, 880hPa, and the probability of occurrence are 10%, 5%, 2%, 1%, 0.1%. The simulation result is displayed through ArcGIS 10.8 software, and the inundation area and depth simulation results for each scenario is shown in Fig. 6. It is seen that the inundation area is spread over the coastal area in southwest of study area. In particular, for the 1000-year return period scenario, the inundation area exceeds 13 km^2 in the study area. Moreover, the presence of Double-Moon Bay leads to the extension of the inundation along the bay, contributing to severe disasters inland.

From the point of view of different scenarios, the area of inundation in direct proportion to the typhoon's return period, and the proportion of inundation area increases from 14% to 31% of study area. When the return period is less than 50 years, most of the flooded area is considered to be in a high-level hazard zone, accounting for 75% for a 10-year return period and 67% for a 20-year return period, and no zone in very high-level hazard. Basically, the inundation area covers land such as grassland, saline land, and some buildings near the estuary as the area is more susceptible to flooding because of the lower elevation and drainage from the estuary. As the return period goes up to 100 years, 34% and 36% of the flooded area are defined at a high-level hazard and very high-level hazard. When it's 1000-year, the situation worsens with approximately half of the inundation area being considered in very high-level hazard. Typically, the flood extends from the margin of terrene, however, the southernmost region of the investigated area is characterized by a knoll covered by forest vegetation, which serves the dual purpose of water absorption and flood mitigation. In addition, the construction of embankments on both sides of Double-Moon Bay effectively withstands flooding. Nevertheless, because of the presence of the estuary, inadequate water absorption ability of coastal saline soil and the hydrological system, the inundation flows in through the estuary and spreads inland.
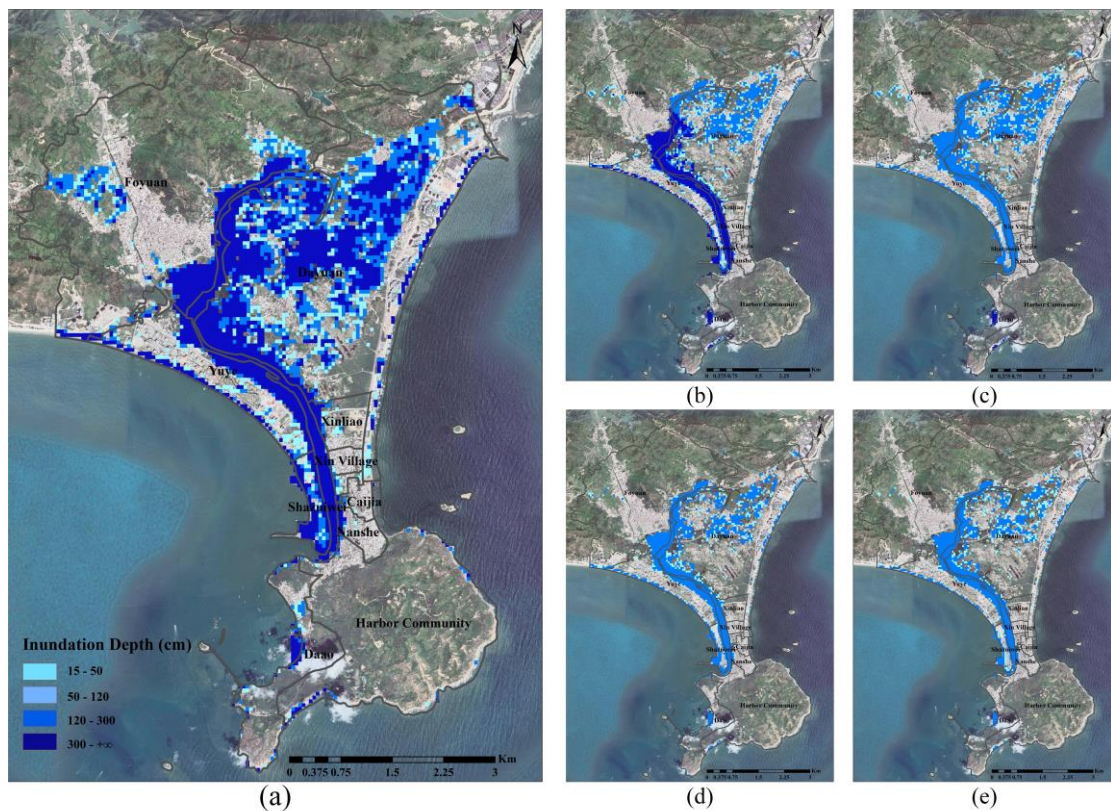
Fig. 6. The storm surge inundation simulation results of five different typhoon scenarios: return period (a) 1000-year, (b): 100-year, (c): 50-year, (d): 20-year, (e): 10-year. The base map is obtained from © GoogleMaps (map data © 2023 Google).

4.2. Buildings' characters extraction

4.2.1 TransUNet model training

The dataset construction area is chosen at southwest waterfront region of Renshan Town. The

498 specific location is shown in Fig. 7. The chosen area is a typical area of the Huizhou coastal area.
499 Apart from the seaside bungalows, the area contains some high-rise buildings that are identified as
500 commercial hotels or resorts, while dense residential area is also widely distributed throughout the
501 inland region. In conclusion, the chosen area contains different kinds of buildings with strong
502 representativeness. Since most of the buildings in China coastal towns have the similar characters,
503 the model trained on the representative region has the ability to identify buildings in other regions
504 rapidly.

505   The labels of the buildings in the area are generated by manually annotation, and the image is
506 cropped into small patches with a size of 256*256. Besides, some of the images without buildings
507 are filtered for preventing the effect of imbalance between the building samples and background
508 samples. In the end, a total of 1200 labeled building dataset is constructed, and the dataset size is
509 deemed sufficient when compared to previous study (Dixit et al., 2021; Ji et al., 2018). The dataset
510 is then divided into a training set and a test set, with the ratio of 8:2. Data enhancement techniques,
511 such as random hue saturation value, random shift scale rotation, flip, and rotation, are
512 implemented during model training to improve the deep learning model's generalization
513 performance and prevent overfitting.

514   The training's initial learning rate is set to 1e-5, and the learning rate adjustment strategy for
515 improved training. The batch size is specified as 4, and the number of training epoch is 100. The
516 model is trained on a NVIDIA RTX3060 GPUs.
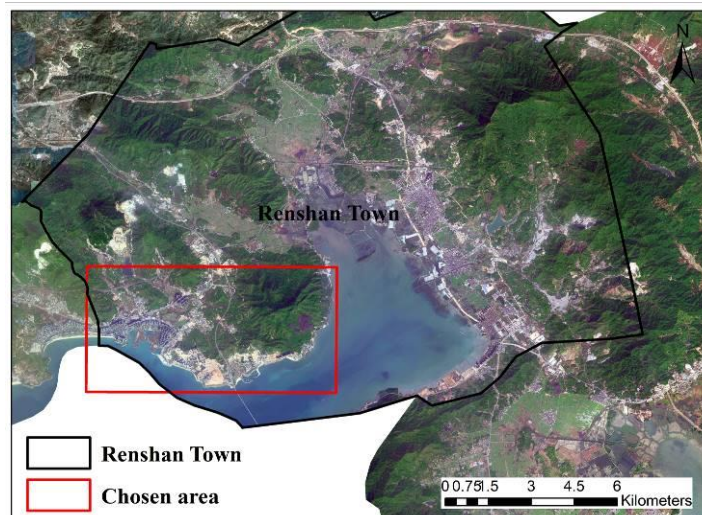
517

518   **Fig. 7.** The chosen area to make the training samples. The base map is obtained from ©
519   GoogleMaps (map data © 2023 Google).

520

521 *4.2.2. Extraction result*

522   Several effective indicators are introduced, including Recall, Precision, F1-score, and mean
523 Intersection-over-Union (mIoU), to evaluate the performance of the deep learning model. Recall is
524 the probability of being predicted as positive among actual positive samples. Precision, on the
525 other hand, is the probability of being actually positive among samples predicted as positive. F1-
526 score serves as an indicator that achieves a balance point between precision and recall, essentially
527 being the harmonic average of precision and recall. mIoU is the mean ratio of the intersection to
528 the union between predicted and true values for each category. True positive (TP) indicates the
529 true samples that are predicted correctly by the model. False positive (FP) indicates the positive
530 samples that the model incorrectly predicted. True negative (TN) and false negative (FN) refer to

531 the number of samples that are correctly and incorrectly predicted as negative by the model. The
532 equations of Recall, Precision, F1-score, and mIoU are as follows:

$$recall = \frac{TP}{TP + FN} \tag{4.1}$$

$$precision = \frac{TP}{TP + FP} \tag{4.2}$$

$$F1 = 2 \times \frac{precision \times recall}{precision + recall} \tag{4.3}$$

$$mIoU = \frac{1}{k+1} \sum_{i=0}^{k} \frac{TP}{TP + FP + FN} \tag{4.4}$$

533   The quantitative evaluation result is shown in Table 2, and the visualization results are
534 illustrated in Fig. 8. As Table 2 shows, the recall score reaches 87% indicating that most of the true
535 building pixels are predicted correctly, and Precision indicates that 82% of all building pixels are
536 correctly detected. Moreover, both the mIoU score and F1-score exceed 80% manifest that the
537 model can balance well between precision and recall. These results reflect the strong performance
538 of TransUNet in the building extraction task. After post-processing the result, such as boundary
539 simplification, the building vectorization results can be used for further research in risk assessment.
540 The overall result is shown in Fig. 9 (b,c).

541   **Table 2.** The statistical accuracy assessment of building footprint extraction

Evaluation metric	
Recall (%)	87.03
Precision (%)	82.04
F1-score (%)	84.46
mIoU (%)	83.38

(a)   (b)   (c)
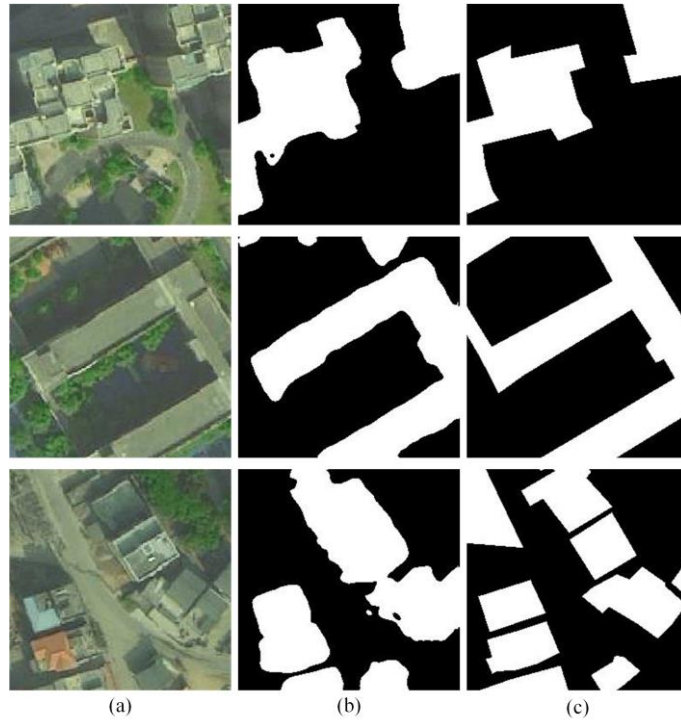
542

543 **Fig. 8.** Building footprint extraction result in study area. (a) Remote sensing images obtained from
544 Jilin-1 satellite (© Chang Guang Satellite technology CO., LTD); (b) Extraction result; (c) Ground
545   truth. The building is marked in white, and the background is marked in black

546

4.2.3. Building height calculation

Through combing two methods mentioned above, the height information is acquired in units of meters. The number of floors is derived by dividing the acquired height information by the specified standard height of 3 meters, according to the China residential design standards. The general condition of building floor is shown in Table 3. Just as mentioned above, the buildings in study area are mainly for residential and commercial use. Since the study area is undeveloped, the high buildings and large mansions is relatively less common, and most of them are built for seaside resort. Instead, buildings with 5 floors or less are the mainstream in study area as respected, which the proportion can reach 76.5%. The building footprint extraction result and building's height information extraction result can be found in Fig. 9 (d,e).

Table 3. Statistical results of building height in the study area

Building floor	Area (m²)	Proportion (%)
1-5	17537238.61	76.5
6-10	4996897.08	21.8
11-20	342207.82	1.5
20+	54083.93	0.2

558
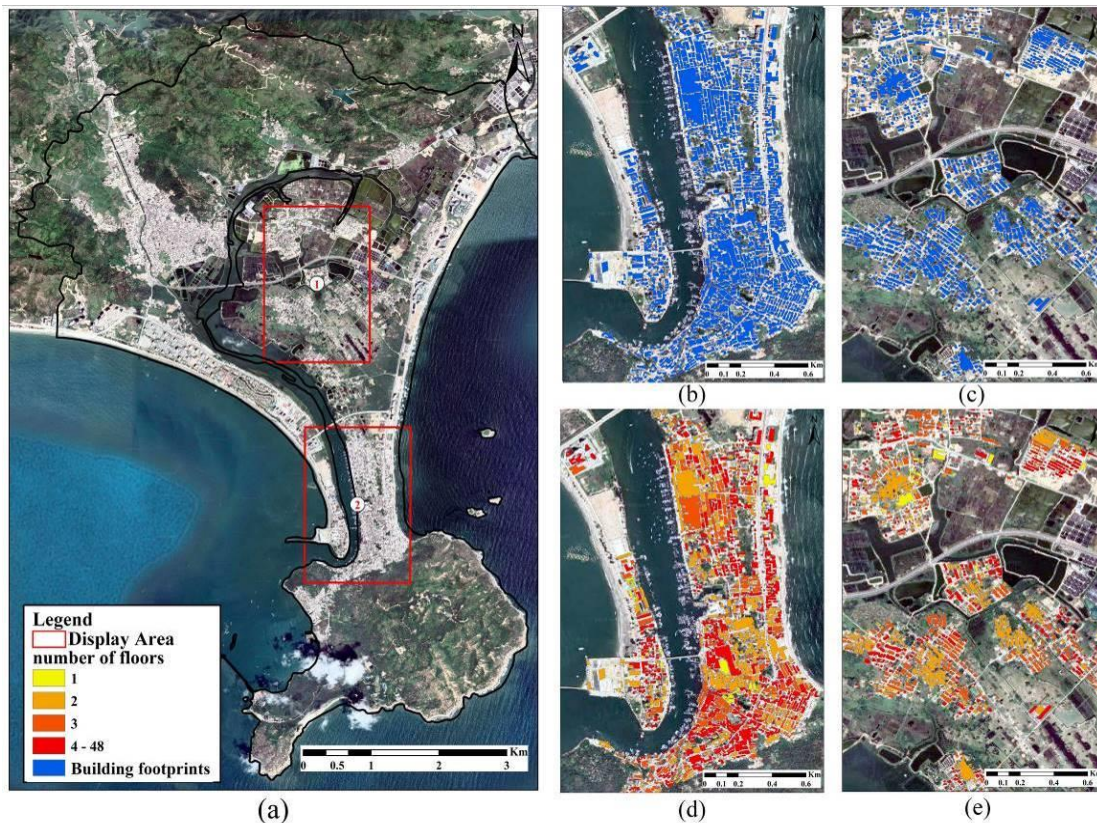
Fig. 9. The building characters extraction result: (a) The schematic of the display area; (b, c) Building footprint result in area 1 and 2; (d, e) Building height result in area 1 and 2. The base map is obtained from © GoogleMaps (map data © 2023 Google).

562

4.3. qualitative risk assessment

Risk matrix is a risk assessment approach firstly developed by Electronic System Center,

565 which was originally to assess the risk in the life cycle of purchase project (Garvey and
566 Lansdowne, 1998). An additional qualitative risk assessment is conducted using the risk matrix
567 method, incorporating improved land use data to highlight the superiority of building extraction in
568 flood risk assessment. The concrete representation of the risk matrix is shown in table 4.

569 **Table 4.** The concrete representation of the risk matrix

		Vulnerability			
		Low	Moderate	High	Very High
Hazard	Low	Low	Low	Moderate	Moderate
	Moderate	Low	Moderate	High	High
	High	Moderate	High	High	Very High
	Very High	Moderate	High	Very High	Very High

570

571   As is shown in Fig. 10(a), the concentrations of organic town of Dayuan village and
572 Shazuiwei makes it in very high vulnerability level. Under the circumstance of defined 880hPa
573 storm surge scenario, the inundation area spread inland which makes the majority area of Dayuan
574 is regarded as moderate risk, and a fraction of the only very high risk area is distributed in
575 Shazuiwei and north of Dayuan village. In the area of Yuye village, part of the south coastal area is
576 considered in moderate or high risk level. That is mainly because the majority area of Yuye is
577 defined as resort district except for a few areas of tidal flats, which is in high vulnerability.
578 However, after referring to the result of hazard assessment, buildings in the area are not actually
579 inundated, meaning the area should not be at risk level.

580   Through comparing the Fig. 10(a) and Fig. 10(b), the enhanced land use data in the present
581 research demonstrates a higher ability to recognize vulnerability elements, which the type is
582 buildings in the present research. The two red boxes in the figure highlight the noticeable disparity
583 between the original and current results. The present risk assessment provides more refined risk
584 assessment result compared to the original result, as the previously identified large hazardous
585 areas are replaced with more detailed and smaller zones. This refinement is conducive for
586 government or decision-makers to conduct disaster prevention measures, propose quick guidance
587 for personnel evacuation and organize rescue operations in the event of a disaster.

<p style="text-align:center;">(a)   (b)</p>
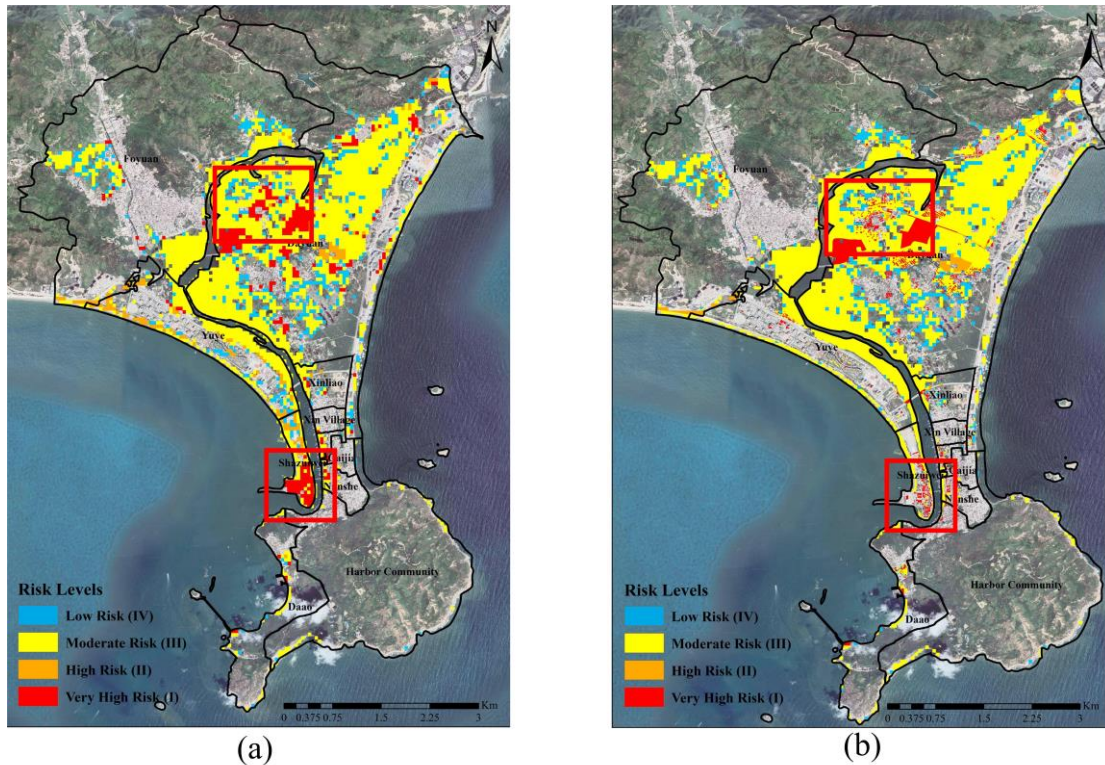
588

589 **Fig. 10.** The risk assessment maps before (a) and after (b) improvement for storm surge scenarios

590 of 1000-year return period. The base map is obtained from © GoogleMaps (map data © 2023

591 Google).

592

593 *4.4. JRC's depth-damage function adaption*

594 Fig. 11 illustrates the damage ratio given flood-depth after adjustment, respectively for one-,

595 two- and more than three-story residential buildings. After adjustment, the damage of one-story

596 residential building function is significantly enhanced, and the loss ratio reach 1 early, which is

597 explicable as 2m-depth flood almost submerges the entire building, resulting in a potential loss of

598 the maximum property value. On the contrary, the loss ratio for multi-story residential building is

599 decreased relative to the original function, it reaches the same level as in the original function

600 when the water depth reaches 5 meters. Furthermore, the function of a two-story residential

601 building is quite similar to that of a building with three or more stories. This can be attributed to

602 the flood's effect on buildings with six meters or less depth being nearly the same, on account of

603 the flood can't overwhelm the entire buildings.

604 The Joint Research Centre provides information on the maximum damages per square for

605 each type of building. This refers to the maximum monetary damage incurred when buildings are

606 inundated, which is the monetary damage value when the damage ratio in the depth-damage curve

607 reaches 100%. Although the maximum monetary damages are provided, they are computed for

608 Beijing in 2010. However, there is a substantial difference in the level of development between

609 Beijing and the study area. For better matching the financial level in study area, adjustment can be

610 achieved based on scaling the maximum monetary damage value with the GDP ratio according to

611 Huizinga (2007). Based on the 2010 GDP of Beijing of 14113558 million yuan and the GDP of

612 Huizhou of 172995 million yuan, the maximum monetary damage is adjusted by equal proportions.

613 Besides, the price level also needs to be adjusted to the 2022 price level. According to the World

614   Bank, the Chinese consumer price index (CPI) has changed from 100 in 2010 to 131.9 in 2022, the

615   tendency of variation and the adjusted maximum monetary damages are shown in Fig. 12.

616

617   (a)   (b)
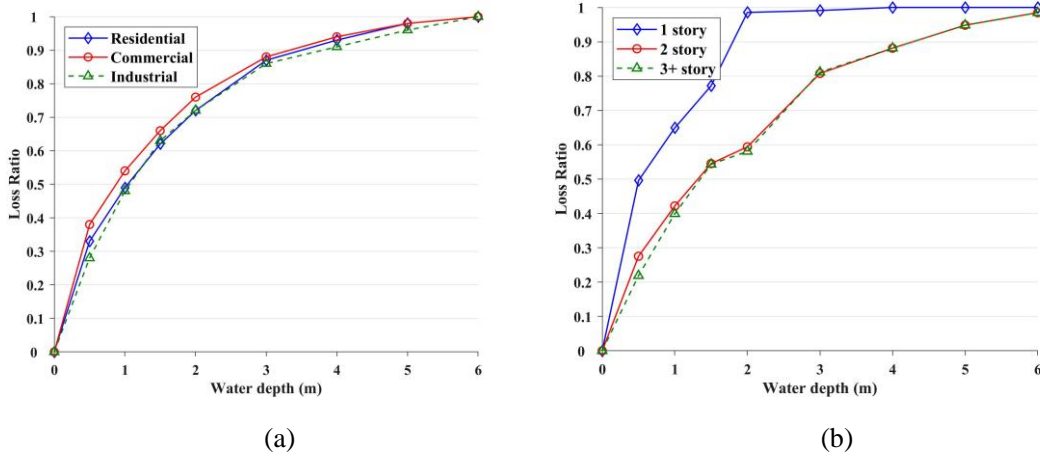
618   **Fig. 11.** (a) The depth-damage functions proposed by JRC; (b) The adapted depth-damage

619   functions for residential buildings in different floors

620

621   (a)   (b)
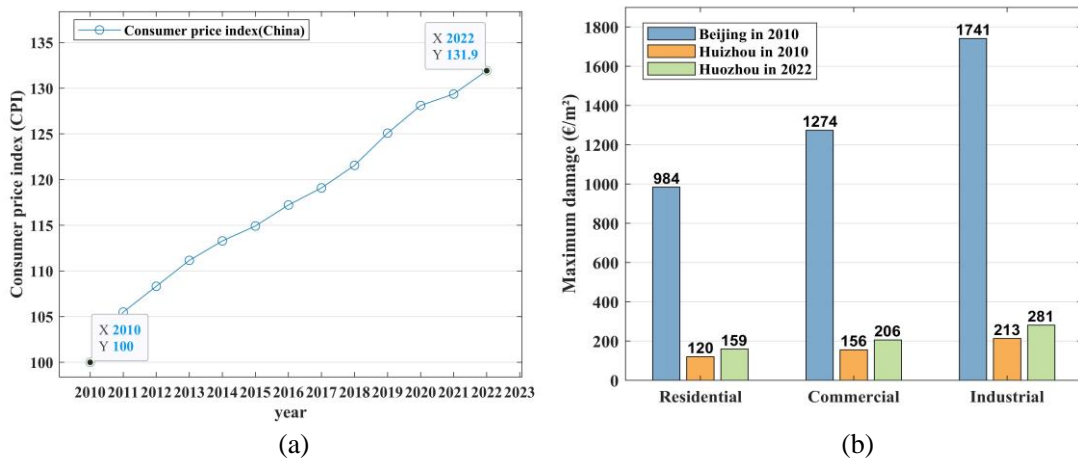
622   **Fig. 12.** (a) The variation trend of Consumer price index released by World Bank; (b) The

623   maximum monetary damage per m^2 for each type of exposed elements in China (in 2010 and in

624   2022).

625

626   *4.5. Quantitative risk assessment*

627   Loss assessments of five storm surge scenarios are computed for return periods of 10, 20, 50,

628   100, and 1000 years, through employing the method in section 3. The estimate monetary damage

629   is summarized in Table 5.

630   The statistical data in Table 5 demonstrate an increase in the affected area and total economic

631   loss with an increasing return period. Comparing to the total affected area of 131533.12 m^2 and

632   the total economic losses of 9330517.49 euros with the 10-year return period, the

633   corresponding estimate result with 1000-year return period is 917437.99 m^2 and 68364923.25

634   euros, which is both approximately seven times higher. This indicates a proportional

635   relationship between the extent of regional impairment and the return period of a typhoon.

636   Although the impacted area for the 20-year and 50-year return periods exhibits relative

637   proximity as the different is 24118.26 m^2, there is still a significant disparity in economic

losses. According to the inundation result above, that's because the inundation area of two return period is nearly the same except for the slight difference in the northeast of the study region, but the flood depth of 50-year intensified, which causes more monetary damage. In terms of inundated building types, in case that study area is characterized as a tourism and fish breeding area, the proportion of economic losses in industrial is relatively low. The losses of residential buildings and commercial buildings is comparatively close, up until the severity of storm surge reach 50-year return period. At this point, the losses experienced by residential buildings exceed those incurred by commercial buildings by more than double. The fact can be explained by the commercial buildings area mainly constructed by the seaside for better turnover therefore both types of waterfront buildings is impacted. However, as the severity of the typhoon worsens, more residential settlements inland are flooded, resulting in a swift increase in economic losses for residential buildings.

Table 5. The statistic result of the quantitative risk assessment for five defined typhoon scenarios.

Scenario	Elements	Area (m^2)	Economic losses (€)	Total losses (€)	Probability	Risk (€)
10-year (940hPa)	Residential	94847.11	4910882.27	9330517.49	0.1	933051.75
	Commercial	36163.62	4281840.09			
	Industrial	522.39	137795.12			
20-year (930hPa)	Residential	216010.31	7872861.19	13665211.91	0.05	683260.60
	Commercial	55423.59	5602828.01			
	Industrial	522.39	189522.71			
50-year (920hPa)	Residential	237572.35	16509796.15	24607011.73	0.02	492140.23
	Commercial	57979.81	7775321.70			
	Industrial	522.39	321893.88			
100-year (910hPa)	Residential	291759.48	19857901.69	28446797.47	0.01	284467.97
	Commercial	75123.51	8194736.70			
	Industrial	833.39	394159.08			
1000-year (880hPa)	Residential	762570.09	49295364.67	68364923.25	0.001	68364.92
	Commercial	149457.01	17907591.59			
	Industrial	5410.89	1161967.00			

Based on the economic losses estimation result for five storm surge scenarios, through using zonal statistics method on the data of administrative sub-zones in the study area, the quantitative risk assessment is conducted. The economic losses and spatial distribution of storm surge risk for ten sub-zones in five different scenarios are shown in Fig. 13. The zonation statistics result map of each sub-zone is defined at four different risk levels (very high, high, moderate, low). The classification of risk levels is obtained by categorizing all zonal statistic result based on quantiles.

As is shown in Fig. 13, Dayuan village is considered in very high risk for every defined typhoon scenario. Through analyzing the geographical characteristics of the study area, it can be found that although Dayuan is a relatively inland village, it's surrounded by the watercourse of the estuary of Double-Moon Bay. Due to the existence of flood control dam, both side of the bay offer a measure of protective effectiveness, which result in the water level rises in inland watercourse, and further causes flooding of residential buildings in Dayuan village, leading to massive financial losses. In contrast, Foyuan village is also a village with a relatively large area, the risk is at moderate level for 10, 20-year return period, and the level escalates to high for 50, 100-year return

period and reaches very high in 1000-year. Considering the presence of the knoll, the spread of inundation is hindered. However, as typhoon becomes more severe, the inundation hit the western buildings in the region, which led to the phenomenon of progressively escalating risk level. In terms of those villages with relatively smaller sizes, due to the protection of dam, Xinliao village, Xin village, Caijia village all are defined in relatively low risk level, although the regions with a high density of buildings. Shazuiwei and Yuye village in different return period are considered in different risk level, the cause of this phenomenon might be that apart from the higher density of buildings, the buildings in Shazuiwei are distributed in coastal area, combing the impact of inundation of both sides as it's located at the outermost part of the gulf. Consequently, the risk level in Shazuiwei remains consistently high as opposed to gradually increasing like in Yuye village. Although they are located at the outermost part of the study area, the quantitative risk level of Daao village and Harbor community is gradually increasing for different return period, but it's not as serious as the other village, which can be explained that these locations exhibit elevated topography.

Comparing the qualitative risk assessment result and the quantitative risk assessment result, the first difference to be noticed is that the two results focus on different scales. For the qualitative result, the emphasis is on delineating the regions in different risk levels, which leads to the prevention and control of priority areas. Whereas for quantitative result, the scale of the result is limited to the village level zoning, as the estimated monetary loss amounts are summarized at the village level. Furthermore, while the qualitative results suggest that certain regions may not be at a moderate or high risk level, the quantitative result reveals that the estimated monetary loss for those villages are not insignificant. In conclude, the qualitative risk assessment provides new results from a completely different perspective than qualitative risk assessment. The results can provide intuitive information about the potential monetary loss to the secondary government departments, thus to help provide constructive suggestions in terms of risk prevention and control.

The quantitative risk assessment and zonal risk maps can assist the government or decision-makers in recognizing the specific economic losses of each sub-zones, so it's helpful to identify the areas that are more susceptible to experiencing significant losses, which allows them to develop disaster prevention measures, for example constructing disaster prevention facilities, budget allocation for disaster prevention and planning evacuation strategies. Besides, establishing the quantitative risk for different typhoon periods can enhance the decision makers understanding of the potential vulnerability in each sub-zone, and facilitates the implementation of appropriate preventive and disaster relief measures facing different typhoon intensity.

699
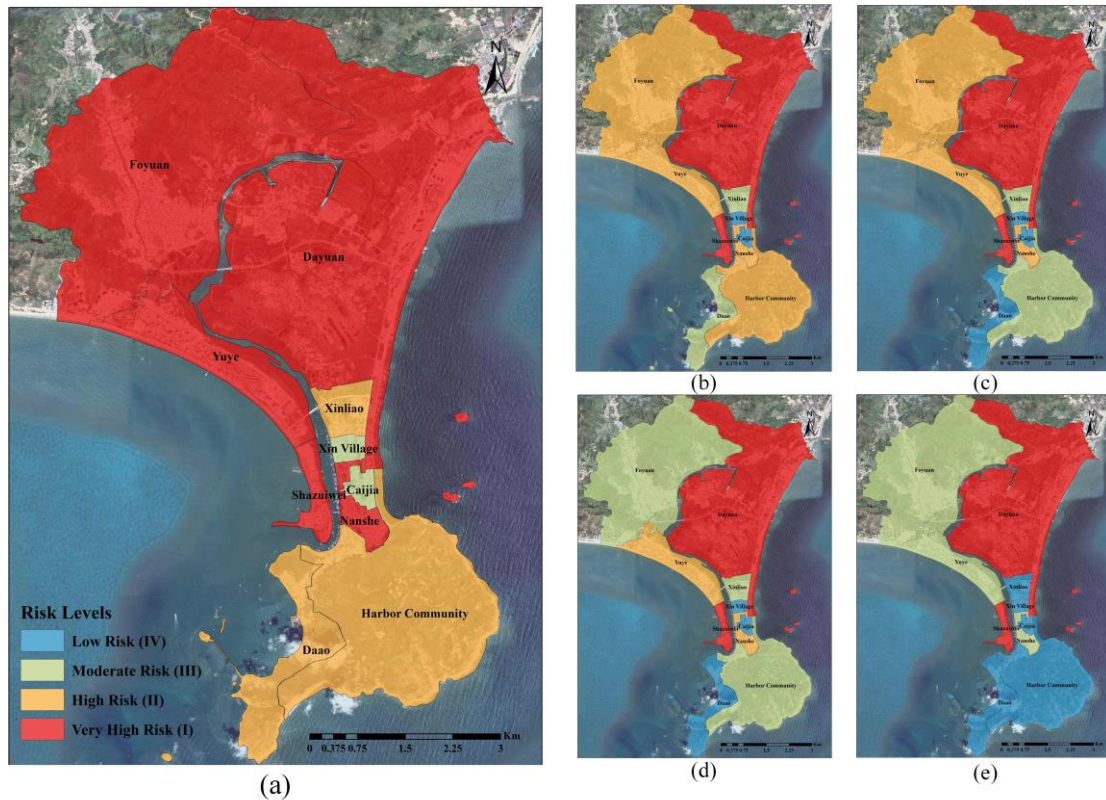
Fig. 13. The zonation maps of the quantitative risk assessment for five defined typhoon scenarios: return period (a) 1000-year, (b): 100-year, (c): 50-year, (d): 20-year, (e): 10-year. The base map is obtained from © GoogleMaps (map data © 2023 Google).

5. Conclusions

These years, the academic research on storm surge risk assessment has been greatly developed due to climate change and financial growth in coastal area. However, the quantitative risk assessment is inexecutable in the undeveloped area since on account of the lacks of building characters and damage assessment data. Target at the question above, the purpose of this paper is to propose a method for conducting refined storm surge risk assessment quantitatively based on deep learning and GIS techniques. Firstly, the reliable coupled FVCOM-SWAN model is utilized to simulate five defined storm surge scenarios. Facing the challenge of the absence of data, a deep learning method TransUNet is applied to extract the building footprint data for refined extraction of exposed elements, and buildings' height data is acquired through UAV. To compensate for that the available depth-damage functions do not taking building's height into account, the functions are adjusted for buildings with different floor and consequently to perform more refined monetary losses calculations in five defined scenarios. Eventually, the quantitative risk assessment and zonation maps of the study area are generated base on GIS techniques

The quantitative risk assessment result of the study region shows that on account of the existence of estuary and the gathering of buildings, Dayuan village presents the high-risk level in all defined typhoon scenario, and the economic loss risk is large. The flood control dam provides protection of Xinliao village, Xin village, Caijia village, which prevents the regions suffering large economic losses as the typhoon return period is 10-year and 20-year. However, the storm surges, under the typhoon scenarios that the return period is greater than 50-year, can overwhelm the existed dikes, and both the commercial buildings and residential buildings suffer heavy economic

losses. Therefore, it's necessary to make land use planning and adjustment especially in Dayuan and Shazuiwei as they are under very high-risk level to prevent the impact and losses caused by storm surges. Besides, the regions that is nearest to the sea doesn't mean they suffer greater potential economic loss, as the risk level of Daao village and Harbor community are considered at a relatively low level because of the topographical characteristics and the distribution of buildings.

In the context of global warming and increased climate extremes, the occurrence of large-scale typhoons has become more frequent, such as Typhoon Rammasun and Typhoon Meranti (corresponding to 100-year return period). Therefore, the modified typhoon parameters are utilized for simulation five typhoon scenarios, in order to assuming the different storm surge disaster situation in the future. On the basis of the above, the study provides a framework for refined quantitative storm surge risk assessment targeting the problem of acquiring exposure elements and the establishing multi-variable empirical depth-damage functions, as a consequence of missing data in underdeveloped regions. The generated results can help the decision-makers to identify the areas that are susceptible to experiencing significant losses efficiently, and help the respective authorities with disaster prevention, future land use planning and material deployment. Furthermore, it is important to remark that, the methodology of this paper has general applicability, since the applied models are publicly available. Thus, there is also potential for further application. For example, the framework can be applied in other coastal areas in China, as they have similar characters, which also means there is a possibility to utilize in larger scales. Furthermore, the framework can also be performed in other types of disasters, such as flood, earthquake, and mudslide. Consequently, the proposed methodology demonstrates an extensive relevance to the scientific community.

There is still room for improvement in this study. The current study relied on manual labeling in terms of distinguishing between functional areas to conduct risk assessment. In the future study, efforts will be made to distinguish the types of exposure elements in a more objective way, based on diverse data sources such as social media Point Of Interest (POI). Additionally, exploring the activity patterns of the population through multiple sources of data including taxi trajectories and smart cards can contribute to the consideration of population risks in different storm surge scenarios, thereby prompting more comprehensive risk assessments.

Data availability.

Remote sensing images are obtained from Chang Guang Jilin-1 satellite. The dataset of wind field is generated by ERA5 and Holland method. The Administrative Boundary data is obtained from National geographic information public service platform. The datasets can be obtained from https://dx.doi.org/10.6084/m9.figshare.24586605 (Yu, 2023). DEM data and UAV data are obtained from Department of Natural Resources of Huizhou Bureau, data sets are not publicly available due to the policy of the Natural Resources of Huizhou Bureau.

Competing interests. The authors declare that they have no conflict of interest.

Authorship contributions.

Lichen Yu: Investigation, Methodology, Data Curation, Visualization, Formal analysis, Writing - Original Draft. **Shining Huang**: Investigation, Data Source, Data Curation, Visualization, Formal analysis. **Hao Qin**: Conceptualization, Methodology, Validation, Supervision, Writing - Original

Draft, Project administration, Funding acquisition. **Wei Wei**: Validation, Data Curation, Visualization. **Lin Mu**: Conceptualization, Supervision, Project administration, Funding acquisition.

Acknowledgement

This work was supported by Shenzhen Science and Technology Program (Grant No. KCXFZ20211020164015024), National Natural Science Foundation of China (Grant No. 52101332) and Guangdong Basic and Applied Basic Research Foundation (Grant No. 2024A1515011805, 2023A1515240047, 2024A1515012032).

References

Adnan, M. S. G., Abdullah, A. Y. M., Dewan, A., and Hall, J. W.: The effects of changing land use and flood hazard on poverty in coastal Bangladesh, Land Use Policy, 99, 104868, 2020.

Armenakis, C. and Nirupama, N.: Estimating spatial disaster risk in urban environments, Geomatics, natural hazards and risk, 4, 289-298, 2013.

Booij, N., Holthuijsen, L. H., and Ris, R. C.: The" SWAN" wave model for shallow water, in, 668-676, 1996.

Chen, C., Liu, H., and Beardsley, R. C.: An unstructured grid, finite-volume, three-dimensional, primitive equations ocean model: application to coastal ocean and estuaries, Journal of atmospheric and oceanic technology, 20, 159-186, 2003.

Chen, D. and Gao, G. X.: Probabilistic graphical fusion of LiDAR, GPS, and 3D building maps for urban UAV navigation, Navigation, 66, 151-168, 2019.

Chen, J., Lu, Y., Yu, Q., Luo, X., Adeli, E., Wang, Y., Lu, L., Yuille, A. L., and Zhou, Y.: Transunet: Transformers make strong encoders for medical image segmentation, arXiv preprint arXiv:2102.04306, 2021.

China Marine disaster bulletin: Historical Marine disasters in China,available at: http://www.mnr.gov.cn/sj/sjfw/hy/gbgg/zghyzhgb/, last access: 12 November 2023.

Comber, A., Umezaki, M., Zhou, R., Ding, Y., Li, Y., Fu, H., Jiang, H., and Tewkesbury, A.: Using shadows in high-resolution imagery to determine building height, Remote Sensing Letters, 3, 551-556, 10.1080/01431161.2011.635161, 2011.

Dabbeek, J., Silva, V., Galasso, C., and Smith, A.: Probabilistic earthquake and flood loss assessment in the Middle East, International Journal of Disaster Risk Reduction, 49, 101662, 2020.

de Moel, H. and Aerts, J. C. J. H.: Effect of uncertainty in land use, damage models and inundation depth on flood damage estimates, Natural Hazards, 58, 407-425, 2011.

Dixit, M., Chaurasia, K., and Kumar Mishra, V.: Dilated-ResUnet: A novel deep learning architecture for building extraction from medium resolution multi-spectral satellite imagery, Expert Systems with Applications, 184, 115530, 2021.

Fang, J., Wahl, T., Fang, J., Sun, X., Kong, F., and Liu, M.: Compound flood potential from storm surge and heavy precipitation in coastal China: dependence, drivers, and impacts, Hydrology and Earth System Sciences, 2021.

Frantz, D., Schug, F., Okujeni, A., Navacchi, C., Wagner, W., van der Linden, S., and Hostert, P.: National-scale mapping of building height using Sentinel-1 and Sentinel-2 time series, Remote Sens Environ, 252, 112128, 10.1016/j.rse.2020.112128, 2021.

Gacu, J. G., Monjardin, C. E. F., de Jesus, K. L. M., and Senoro, D. B.: GIS-Based Risk Assessment of

Structure Attributes in Flood Zones of Odiongan, Romblon, Philippines, Buildings, 13, 506, 2023.

Garvey, P. R. and Lansdowne, Z. F.: Risk matrix: an approach for identifying, assessing, and ranking program risks, Air Force Journal of Logistics, 22, 18-21, 1998.

Glahn, B., Taylor, A., Kurkowski, N., and Shaffer, W. A. J. N. W. D.: The role of the SLOSH model in National Weather Service storm surge forecasting, 33, 3-14, 2009.

Grahn, T. and Nyberg, R.: Damage assessment of lake floods: Insured damage to private property during two lake floods in Sweden 2000/2001, International journal of disaster risk reduction, 10, 305-314, 2014.

Granger, K.: Quantifying storm tide risk in Cairns, Natural Hazards, 30, 165-185, 2003.

Hasanzadeh Nafari, R., Ngo, T., and Lehman, W.: Calibration and validation of FLFA_{rs} -- a new flood loss function for Australian residential structures, Natural Hazards and Earth System Sciences, 16, 15-27, 10.5194/nhess-16-15-2016, 2016.

Hess, T. M. and Morris, J.: Estimating the value of flood alleviation on agricultural grassland, Agricultural Water Management, 15, 141-153, 1988.

Holland, G. J.: An analytic model of the wind and pressure profiles in hurricanes, 1980.

Hu, K., Meselhe, E., Rhode, R., Snider, N., and Renfro, A.: The Impact of Levee Openings on Storm Surge: A Numerical Analysis in Coastal Louisiana, Applied Sciences, 12, 10884, 2022.

Huang, H., Chen, P., Xu, X., Liu, C., Wang, J., Liu, C., Clinton, N., and Gong, P.: Estimating building height in China from ALOS AW3D30, ISPRS Journal of Photogrammetry and Remote Sensing, 185, 146-157, 10.1016/j.isprsjprs.2022.01.022, 2022.

Huizinga, J., De Moel, H., and Szewczyk, W.: Global flood depth-damage functions: Methodology and the database with guidelines, 2017.

Ji, S., Wei, S., and Lu, M.: Fully convolutional networks for multisource building extraction from an open aerial and satellite imagery data set, IEEE Transactions on geoscience and remote sensing, 57, 574-586, 2018.

Ji, T., Li, G., Liu, Y., Liu, R., and Zhu, Y.: Spatiotemporal Features of Storm Surge Activity and Its Response to Climate Change in the Southeastern Coastal Area of China in the Past 60 years, Journal of Geophysical Research: Atmospheres, 126, 2020.

Kang, C. L., Cheng, Y., Wang, F., Zong, M. M., Luo, J., and Lei, J. Y.: THE APPLICATION OF UAV OBLIQUE PHOTOGRAMMETRY IN SMART TOURISM: A CASE STUDY OF LONGJI TERRACED SCENIC SPOT IN GUANGXI PROVINCE, The International Archives of the Photogrammetry, Remote Sensing and Spatial Information Sciences, XLII-3/W10, 575-580, 2020.

Kreibich, H., Seifert, I., Merz, B., and Thieken, A. H.: Development of FLEMOcs – a new model for the estimation of flood losses in the commercial sector, Hydrological Sciences Journal, 55, 1302-1314, 2010.

Kron, W.: Flood risk= hazard• values• vulnerability, Water international, 30, 58-68, 2005.

Lee, J.: The economic aftermath of Hurricanes Harvey and Irma: The role of federal aid, International journal of disaster risk reduction, 61, 102301, 2021.

Li, X., Zhou, Y., Gong, P., Seto, K. C., and Clinton, N.: Developing a method to estimate building height from Sentinel-1 data, Remote Sensing of Environment, 240, 10.1016/j.rse.2020.111705, 2020.

Liu, W.-C. and Huang, W.-C.: Investigating typhoon-induced storm surge and waves in the coast of Taiwan using an integrally-coupled tide-surge-wave model, Ocean Engineering, 212, 107571, 2020.

Liu, Y., Li, Z., Wei, B., Li, X., and Fu, B.: Seismic vulnerability assessment at urban scale using data mining and GIScience technology: application to Urumqi (China), Geomatics, Natural Hazards and

Risk, 10, 958-985, 2019.

Liu, Y., So, E., Li, Z., Su, G., Gross, L., Li, X., Qi, W., Yang, F., Fu, B., and Yalikun, A.: Scenario-based seismic vulnerability and hazard analyses to help direct disaster risk reduction in rural Weinan, China, International Journal of Disaster Risk Reduction, 48, 101577, 2020.

Lyddon, C. E., Brown, J. M., Leonardi, N., Saulter, A., and Plater, A. J.: Quantification of the Uncertainty in Coastal Storm Hazard Predictions Due to Wave-Current Interaction and Wind Forcing, Geophysical Research Letters, 46, 14576-14585, 2019.

Malekinezhad, H., Sepehri, M., Pham, Q. B., Hosseini, S. Z., Meshram, S. G., Vojtek, M., and Vojteková, J.: Application of entropy weighting method for urban flood hazard mapping, Acta Geophysica, 69, 841-854, 2021.

Marvi, M. T.: A review of flood damage analysis for a building structure and contents, Natural Hazards, 102, 967-995, 10.1007/s11069-020-03941-w, 2020.

Masson, D.: A case study of wave–current interaction in a strong tidal current, Journal of physical oceanography, 26, 359-372, 1996.

McGranahan, G., Balk, D., and Anderson, B.: The rising tide: assessing the risks of climate change and human settlements in low elevation coastal zones, Environment and urbanization, 19, 17-37, 2007.

McPherson, M.: Responding to Typhoon Haiyan in the Philippines, Western Pacific Surveillance and Response Journal, 6, 1-4, 2015.

Merz, B., Kreibich, H., and Lall, U.: Multi-variate flood damage assessment: a tree-based data-mining approach, Natural Hazards and Earth System Sciences, 13, 53-64, 2013.

Merz, B., Thieken, A. H., and Gocht, M.: Flood risk mapping at the local scale: concepts and challenges, Flood risk management in Europe: innovation in policy and practice, 231-251, 2007.

Mharzi Alaoui, H., Radoine, H., Chenal, J., Hajji, H., and Yakubu, H.: Deep building footprint extraction for urban risk assessment–Remote sensing and Deep learning based approach, The International Archives of the Photogrammetry, Remote Sensing and Spatial Information Sciences, 48, 83-86, 2022.

Nastev, M. and Todorov, N.: Hazus: A standardized methodology for flood risk assessment in Canada, Canadian Water Resources Journal, 38, 223-231, 2013.

Paprotny, D., Kreibich, H., Morales-Nápoles, O., Castellarin, A., Carisi, F., and Schröter, K.: Exposure and vulnerability estimation for modelling flood losses to commercial assets in Europe, Science of The Total Environment, 737, 140011, 2020.

Pathan, A. I., Girish Agnihotri, P., Said, S., and Patel, D.: AHP and TOPSIS based flood risk assessment- a case study of the Navsari City, Gujarat, India, Environmental Monitoring and Assessment, 194, 2022.

Rafiei-Sardooi, E., Azareh, A., Choubin, B., Mosavi, A. H., and Clague, J. J.: Evaluating urban flood risk using hybrid method of TOPSIS and machine learning, International Journal of Disaster Risk Reduction, 66, 102614, 2021.

Ramkar, P. and Yadav, S. M.: Flood risk index in data-scarce river basins using the AHP and GIS approach, Natural Hazards, 109, 1119-1140, 2021.

Rizzi, J., Torresan, S., Zabeo, A., Critto, A., Tosoni, A., Tomasin, A., and Marcomini, A.: Assessing storm surge risk under future sea-level rise scenarios: a case study in the North Adriatic coast, Journal of Coastal Conservation, 21, 453-471, 10.1007/s11852-017-0517-5, 2017.

Rousell, A. and Zipf, A.: Towards a Landmark-Based Pedestrian Navigation Service Using OSM Data, ISPRS international journal of geo-information, 6, 64, 2017.

Scawthorn, C., Blais, N., Seligson, H., Tate, E., Mifflin, E., Thomas, W., Murphy, J., and Jones, C.: HAZUS-MH flood loss estimation methodology. I: Overview and flood hazard characterization, Natural Hazards Review, 7, 60-71, 2006.

Seto, K. C., Fragkias, M., Güneralp, B., and Reilly, M. K.: A meta-analysis of global urban land expansion, PloS one, 6, e23777, 2011.

Shao, Y., Taff, G. N., and Walsh, S. J.: Shadow detection and building-height estimation using IKONOS data, International Journal of Remote Sensing, 32, 6929-6944, 10.1080/01431161.2010.517226, 2011.

Shi, X., Tan, J., Guo, Z., and Liu, Q.: A review of risk assessment of storm surge disaster, Advances in Earth Science, 28, 866, 2013.

Smith, D. I.: Flood damage estimation - A review of urban stage-damage curves and loss functions, Water S. A., 20, 231-238, 1994.

Sutskever, I., Vinyals, O., and Le, Q. V.: Sequence to sequence learning with neural networks, Advances in neural information processing systems, 27, 2014.

Tang, J., Wang, L., and Yao, Z.: Analyzing urban sprawl spatial fragmentation using multi-temporal satellite images, GIScience & Remote Sensing, 43, 218-232, 2006.

Taramelli, A., Righini, M., Valentini, E., Alfieri, L., Gatti, I., and Gabellani, S.: Building-scale flood loss estimation through vulnerability pattern characterization: application to an urban flood in Milan, Italy, Natural Hazards and Earth System Sciences, 22, 3543-3569, 10.5194/nhess-22-3543-2022, 2022.

Tate, E., Munoz, C., and Suchan, J.: Uncertainty and sensitivity analysis of the HAZUS-MH flood model, Natural Hazards Review, 16, 04014030, 2015.

Thieken, A. H., Olschewski, A., Kreibich, H., Kobsch, S., and Merz, B.: Development and evaluation of FLEMOps – a new Flood Loss Estimation MOdel for the private sector, Flood Recovery, Innovation and Response I, 10.2495/friar080301, 2008.

Vijayan, L., Huang, W., Yin, K., Ozguven, E., Burns, S., and Ghorbanzadeh, M.: Evaluation of parametric wind models for more accurate modeling of storm surge: a case study of Hurricane Michael, Natural Hazards, 106, 2003-2024, 2021.

Wang, N., Hou, Y., Mo, D., and Li, J.: Hazard assessment of storm surges and concomitant waves in Shandong Peninsula based on long-term numerical simulations, Ocean & Coastal Management, 213, 105888, 2021a.

Wang, S., Mu, L., Yao, Z., Gao, J., Zhao, E., and Wang, L.: Assessing and zoning of typhoon storm surge risk with a geographic information system (GIS) technique: a case study of the coastal area of Huizhou, Natural Hazards and Earth System Sciences, 21, 439-462, 10.5194/nhess-21-439-2021, 2021b.

Wu, J., Ye, M., Wang, X., and Koks, E.: Building Asset Value Mapping in Support of Flood Risk Assessments: A Case Study of Shanghai, China, 2019.

Yang, J., Li, L., Zhao, K., Wang, P., Wang, D., Sou, I. M., Yang, Z., Hu, J., Tang, X., Mok, K. M., and Liu, P. L. F.: A Comparative Study of Typhoon Hato (2017) and Typhoon Mangkhut (2018)—Their Impacts on Coastal Inundation in Macau, Journal of Geophysical Research: Oceans, 124, 9590-9619, 10.1029/2019jc015249, 2019.

Yang, Z., Shao, W., Ding, Y., Shi, J., and Ji, Q.: Wave Simulation by the SWAN Model and FVCOM Considering the Sea-Water Level around the Zhoushan Islands, Journal of Marine Science and Engineering, 8, 783, 2020.

Yazdi, J. and Salehi Neyshabouri, S. A. A.: Optimal design of flood-control multi-reservoir system on a

944 watershed scale, Natural hazards (Dordrecht), 63, 629-646, 2012.

945 Yu: NHESS_dataset, 10.6084/m9.figshare.24586605.v2, 2023.

946 Zhai, G., Fukuzono, T., and Ikeda, S.: MODELING FLOOD DAMAGE: CASE OF TOKAI FLOOD

947 20001, Journal of the American Water Resources Association, 41, 77-92, 2005.

948 Zhang, S., Zhang, J., Li, X., Du, X., Zhao, T., Hou, Q., and Jin, X.: Quantitative risk assessment of

949 typhoon storm surge for multi-risk sources, J Environ Manage, 327, 116860,

950 10.1016/j.jenvman.2022.116860, 2023.

951 Zhang, Z., Chen, C., Song, Z., Zhang, D., Hu, D., and Guo, F.: A FVCOM study of the potential coastal

952 flooding in apponagansett bay and clarks cove, Dartmouth Town (MA), Natural Hazards, 103, 2787-

953 2809, 2020.

954 Zhou, C., Chen, P., Yang, S., Zheng, F., Yu, H., Tang, J., Lu, Y., Chen, G., Lu, X., Zhang, X., and Sun,

955 J.: The impact of Typhoon Lekima (2019) on East China: a postevent survey in Wenzhou City and

956 Taizhou City, Frontiers of Earth Science, 16, 109-120, 10.1007/s11707-020-0856-7, 2021.

957 Zhou, G., Song, C., Simmers, J., and Cheng, P.: Urban 3D GIS from LiDAR and digital aerial images,

958 Computers & geosciences, 30, 345-353, 2004.

959 Zhu, T., Ke, S., Li, W., Chen, J., Yun, Y., and Ren, H.: WRF-CFD/CSD analytical method of

960 hydroelastic responses of ultra-large floating body on maritime airport under typhoon-wave-current

961 coupling effect, Ocean Engineering, 261, 112022, 2022.

962